The Astrophysical Journal, 907:52 (19pp), 2021 January 20 https://doi.org/10.3847/1538-4357/abca8a

The Early Discovery of SN 2017ahn: Signatures of Persistent Interaction in a Fast-declining Type II Supernova

L. Tartaglia[1,2], D. J. Sand[3], J. H. Groh[4], S. Valenti[5], S. D. Wyatt[3], K. A. Bostroem[5], P. J. Brown[6], S. Yang[2], J. Burke[7,8], T.-W. Chen[2,9], S. Davis[10], F. Förster[11,12], L. Galbany[13], J. Haislip[14], D. Hiramatsu[7,8], G. Hosseinzadeh[15], D. A. Howell[7,8], E. Y. Hsiao[10], S. W. Jha[16], V. Kouprianov[14], H. Kuncarayakti[17,18], J. D. Lyman[19], C. McCully[7], M. M. Phillips[20], A. Rau[9], D. E. Reichart[14], M. Shahbandeh[10], and J. Strader[21]
[1] INAF—Osservatorio Astronomico di Padova, Vicolo dell'Osservatorio 5, I-35122 Padova, Italy; leonardo.tartaglia@inaf.it
[2] Department of Astronomy and the Oskar Klein Centre, Stockholm University, AlbaNova, Roslagstullsbacken 21, SE-114 21 Stockholm, Sweden
[3] Steward Observatory, University of Arizona, 933 North Cherry Avenue, Rm. N204, Tucson, AZ 85721-0065, USA
[4] School of Physics, Trinity College Dublin, the University of Dublin, Dublin, Ireland
[5] Department of Physics, University of California, 1 Shields Avenue, Davis, CA 95616-5270, USA
[6] Mitchell Institute for Fundamental Physics and Astronomy, Texas A&M University, College Station, TX 77843, USA
[7] Las Cumbres Observatory, 6740 Cortona Drive, Suite 102, Goleta, CA 93117-5575, USA
[8] Department of Physics, University of California, Santa Barbara, CA 93106-9530, USA
[9] Max-Planck-Institut für Extraterrestrische Physik, Giessenbachstraße 1, D-85748, Garching, Germany
[10] Department of Physics, Florida State University, 77 Chieftan Way, Tallahassee, FL 32306, USA
[11] Millennium Institute of Astrophysics (MAS), Nuncio Monseñor Sotero Sanz 100, Providencia, Santiago, Chile
[12] Center for Mathematical Modelling, Universidad de Chile, Avenida Blanco Encalada 2120 Piso7, Santiago, Chile
[13] Departamento de Física Teórica y del Cosmos, Universidad de Granada, E-18071 Granada, Spain
[14] Department of Physics and Astronomy, University of North Carolina at Chapel Hill, Chapel Hill, NC 27599, USA
[15] Center for Astrophysics | Harvard & Smithsonian, 60 Garden Street, Cambridge, MA 02138-1516, USA
[16] Department of Physics and Astronomy, Rutgers the State University of New Jersey, 136 Frelinghuysen Road, Piscataway, NJ 08854, USA
[17] Tuorla Observatory, Department of Physics and Astronomy, FI-20014 University of Turku, Finland
[18] Finnish Centre for Astronomy with ESO (FINCA), FI-20014 University of Turku, Finland
[19] Department of Physics, University of Warwick, Coventry CV4 7AL, UK
[20] Carnegie Observatories, Las Campanas Observatory, Casilla 601, La Serena, Chile
[21] Center for Data Intensive and Time Domain Astronomy, Department of Physics and Astronomy, Michigan State University, East Lansing, MI 48824, USA
Received 2020 August 14; revised 2020 November 12; accepted 2020 November 12; published 2021 January 28

Abstract

We present high-cadence, comprehensive data on the nearby ($D \simeq 33$ Mpc) Type II supernova (SN II) 2017ahn, discovered within about one day of the explosion, from the very early phases after explosion to the nebular phase. The observables of SN 2017ahn show a significant evolution over the ≃470 days of our follow-up campaign, first showing prominent, narrow Balmer lines and other high-ionization features purely in emission (i.e., flash spectroscopy features), which progressively fade and lead to a spectroscopic evolution similar to that of more canonical SNe II. Over the same period, the decline of the light curves in all bands is fast, resembling the photometric evolution of linearly declining H-rich core-collapse SNe. The modeling of the light curves and early flash spectra suggests that a complex circumstellar medium surrounds the progenitor star at the time of explosion, with a first dense shell produced during the very late stages of its evolution that is swept up by the rapidly expanding ejecta within the first ∼6 days of the SN evolution, while signatures of interaction are observed also at later phases. Hydrodynamical models support the scenario in which linearly declining SNe II are predicted to arise from massive yellow super- or hypergiants depleted of most of their hydrogen layers.

Unified Astronomy Thesaurus concepts: Supernovae (1668); Core-collapse supernovae (304); Type II supernovae (1731)

Supporting material: data behind figures, machine-readable tables

1. Introduction

Core-collapse supernovae (CC SNe) are the spectacular endpoint of the evolution of massive stars (>8–9 $M_{\odot}$; Heger et al. 2003; Smartt 2009). Hydrogen-rich SNe are typically labeled Type II SNe (Filippenko 1997; Gal-Yam 2017), which are further classified on the basis of their photometric evolution after peak (Barbon et al. 1979; Li et al. 2011; Smith et al. 2011; Graur et al. 2017). The distinction is made between transients showing a characteristic plateau lasting ≃100 days (see, e.g., Anderson et al. 2014b) and those showing linear or almost linear declines after maximum light (see, e.g., Faran et al. 2014, and references therein). Although this diversity might be solely due to different amounts of H retained at the time of the explosion, different progenitor channels have been proposed for the rare class of SNe IIL (6%–10% of all CC SNe; Li et al. 2011; Smith et al. 2011) and the more common Type IIP SNe. In particular, Type IIL have been proposed to arise from more massive stars that are partially depleted of their outer H layers, with larger radii (a few $10^3\,R_{\odot}$; e.g., Blinnikov & Bartunov 1993) than more compact (<1600 $R_{\odot}$; Levesque et al. 2005) and less massive red supergiants (RSGs) (see, e.g., Elias-Rosa et al. 2010; Fraser et al. 2010; Anderson et al. 2012), although Morozova et al. (2017) showed that RSGs surrounded by dense circumstellar medium (CSM) can also produce the observables of SNe IIL. On the other hand, more recently, a few authors proposed that Type II SNe form a heterogeneous class, with their light curves forming a continuum of properties (Anderson et al. 2014b; Sanders et al. 2015; Galbany et al. 2016;

Rubin & Gal-Yam 2016; Valenti et al. 2016; de Jaeger et al. 2019).

Core-collapes SNe that interact with a dense H-rich CSM typically show narrow features (with a full width at half maximum, FWHM, of a few 10^2 up to a few 10^3 km s^{-1}) and are therefore labeled SNe IIn (Schlegel 1990). These are recombination lines emitted by the outer unshocked CSM, with ionizing photons produced in the underlying shocked regions (see Chevalier & Fransson 1994). Narrow lines, on the other hand, are not the only signature of ongoing interaction of ejecta and CSM: collisions between dense shells are expected to produce boxy, flat-topped profiles (see, e.g., Inserra et al. 2011; Jerkstrand 2017, and references therein), and strong signatures of interaction can be deduced from observations in the X-ray and radio domains of transients not showing narrow emission features (see, e.g., Fransson et al. 1996).

While in "normal" CC SNe the SN shock is expected to break through the stellar photosphere, in stars that explode within a dense medium, this typically occurs within the CSM (see, e.g., Svirski et al. 2012; Förster et al. 2018), leading to a drastic increase in the timescale of the shock breakout signal (Balberg & Loeb 2011). While this signal typically fades within seconds to a fraction of an hour after explosion, in SNe that interact with a dense CSM, this can be extended up to a timescale of days (Balberg & Loeb 2011). This is the case of Type IIn SNe, where the shock can break through the extended CSM up to 100 days after the SN explosion (see, e.g., Tartaglia et al. 2020), as long as the optical depth of the overlying medium is higher than $\simeq c/v$ (where v is the shock expansion velocity). After this time, their photometric evolution is mainly shaped by ongoing interaction of ejecta and CSM, depending on the efficiency in the conversion of kinetic energy into radiation and the density profiles of the SN ejecta and shocked gas (see Chevalier 1982; Moriya et al. 2013; Fransson et al. 2014). Similarly, their spectroscopic evolution can be dominated by interaction up to many years after the SN explosion, with line profiles shaped by electron scattering (see Huang & Chevalier 2018), or occasionally, showing emission components from shocked shells (see, e.g., Taddia et al. 2020). Interaction can mask the underlying ejecta, preventing us from collecting information about the progenitor stars (typically accessible during the nebular phases), and occasionally, even explosion mechanisms (see, e.g., Silverman et al. 2013). This is mainly because the pseudo-photosphere is typically located in the outer unshocked CSM, produced through stationary winds or eruptive events throughout the evolution of the progenitor star, and it only reflects the composition of the outermost layers of its envelope.

On the other hand, in CC SNe that are discovered soon after explosion, narrow features may arise from shells that are expelled during the very late phases of the evolution of their progenitors, and hence reflect the chemical composition of their outer layers just before explosion (see, e.g., the cases of SNe 1983K; Niemela et al. 1985 1993J; Garnavich & Ann 1994; Matheson et al. 2000, 1998S; Leonard et al. 2000; Shivvers et al. 2015, 2006bp Quimby et al. 2007, and the more recent cases of SNe 2013cu; Gal-Yam et al. 2014, 2013fs; Yaron et al. 2017 and 2016bkv; Hosseinzadeh et al. 2018). These high-ionization (e.g., He II, C III–IV, N IV–V and occasionally -VIO IV) features, sometimes dubbed "flash spectroscopy" features, rapidly fade and typically disappear after a few days, depending on the physical conditions of the emitting shell, and on the time in which these regions are overtaken by the rapidly expanding SN ejecta. The occurrence of CC SNe showing early high-ionization features is expected to be relatively high (∼20% of those discovered within 5 days since explosion; Khazov et al. 2016), and their numbers will increase with the advent of modern about one-day cadence SN surveys such as the Palomar Transient Facility (PTF and its continuation iPTF; Law et al. 2009; Kulkarni 2013), the All Sky Automated Survey for SNe (ASAS-SN; Shappee et al. 2014), the Asteroid Terrestrial-Impact Last Alert System (ATLAS; Tonry 2011; Smith et al. 2020), the Distance Less Than 40 Mpc (DLT40; Tartaglia et al. 2018), and the Zwicky Transient Facility (ZTF; Bellm et al. 2019; Graham et al. 2019).

In this context, we present the discovery and the detailed follow-up campaign of the Type II SN 2017ahn. SN 2017ahn was discovered on 2017 February 8.29 UT (Tartaglia et al. 2017) in the nearby galaxy NGC 3318 during the second year of operations of DLT40, which specifically searches for nearby SNe within one day from explosion. It was given the internal designation DLT17h. First detection and the subsequent confirmation image were both obtained using the 0.41 m PROMPT 5 telescope (Reichart et al. 2005) located at the Cerro Tololo Inter-American Observatory (CTIO; Cerro Pachón, Chile). SN 2017ahn was also observed at radio frequencies on 2017 February 28.6 UT (JD = 2457813.1, ≃21 days after explosion) with the Australia Telescope Compact Array (ATCA), resulting in nondetection limits of 75 and 40 μJy beam^{-1} at 5.5 and 9.0 GHz, respectively (Ryder et al. 2017). Further details about the DLT40 survey during the time period of this SN discovery are discussed in Yang et al. (2017, 2019) and Tartaglia et al. (2018).

In Section 2 we discuss the local environment of SN 2017ahn and infer its host extinction, while Section 3 includes details about the photometric (Section 3.1) and spectroscopic (Sections 3.2 and 3.3) follow-up campaigns of SN 2017ahn. In Section 4 we discuss the main observables in the context of young nearby CC SNe, while the main results of our analysis are summarized in Section 5. Additional information about the facilities used to collect data as well as the reduction steps and tools are reported in the appendix.

2. The Local Environment

SN 2017ahn is located at R.A. = 10:37:17.45, decl. = −41:37:05.27 [J2000], 21.″75 E, 33.″93 N from the center of its host galaxy, NGC 3318 (see Figure 1). NGC 3318 is a nearby ($D \lesssim 38$ Mpc[22]) spiral galaxy (SAB(rs)b; de Vaucouleurs et al. 1991), which already hosted the Type II SN 2000cl (Chassagne et al. 2000), 15.″47 W, 42.″51 S away from the position of SN 2017ahn and the Type II SN 2020aze (24.″44 W, 23.″65 S from SN 2017ahn; B. Ailawadhi et al. 2020, in preparation). In the following, we assume a luminosity distance of 33.0 ± 6.5 Mpc to NGC 3318, corresponding to a distance modulus of $\mu = 32.59 \pm 0.43$ mag (as derived by Sorce et al. 2014 using data obtained during the observational campaign Cosmicflows with Spitzer; Courtois & Tully 2012a, 2012b; Tully & Courtois 2012; Tully et al. 2013), placing SN 2017ahn at a projected distance of ≃6.4 kpc from the center of NGC 3318. This value is in agreement with that found by Carrick et al. (2015), resulting in a "cosmicflows-3" luminosity

[22] https://ned.ipac.caltech.edu/

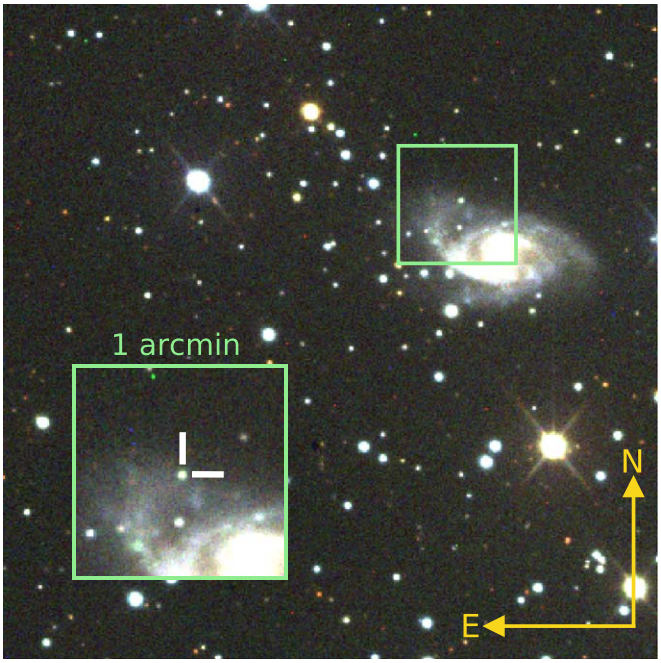

Figure 1. Color image of SN 2017ahn and its host galaxy NGC 3318. The image combined *g*-, *r*-, and *i*-band data obtained on 2017 April 16 (~68 days days after explosion) with a 1 m telescope of the Las Cumbres Observatory network (1m-012, node at the South African Astronomical Observatory—SAAO, Cape Town, South Africa). SN 2017ahn is the bright source in the middle of the inset.

distance $D_L = 40.76$ Mpc (assuming $\Omega_M = 0.3$, $\Omega_\Lambda = 0.7$ and $H_0 = 70$ km s^{-1} Mpc^{-1}), corresponding to a distance modulus $\mu = 33.05 \pm$ mag,[23] as well as that inferred using The Extragalactic Distance Database (EDD;[24] see Kourkchi et al. 2020) based on the linear density field model of Graziani et al. (2019, $\mu = 32.73 \pm 0.21$ mag).

For the foreground Galactic extinction we adopt the values reported by Schlafly & Finkbeiner (2011), corresponding to $E(B - V) = 0.068$ mag, while to estimate the local extinction, we compared results obtained using different methods.

A first estimate was obtained using data collected with the VLT/Multi Unit Spectroscopic Explorer (MUSE; Bacon et al. 2014) integral field spectrograph on 2015 May 17,[25] as part of a survey of nearby SN explosion sites (see Kuncarayakti et al. 2018, for details), which serendipitously included the site of SN 2017ahn in its field of view. Line-of-sight extinction was estimated from the observed Balmer decrement (Hα/Hβ, after correcting the spectrum for the Galactic extinction) of a nearby H II region, assuming an intrinsic flux ratio of 2.86 (Case B recombination; Osterbrock & Ferland 2006) and a standard extinction law with $R_V = 3.1$ (Cardelli et al. 1989), yielding an additional contribution of $E(B - V) = 0.09 \pm 0.06$ mag from the local environment.

On the other hand, a rapid inspection of the 5800–6000 Å region in our spectrum obtained on 2017 March 15 (36 days after explosion, see Section 3) reveals host DNa I features much stronger than the those due to the Galactic extinction, with a total equivalent width $EW_{host} \simeq 2.6 \times EW_{MW}$, as measured from the overall profile including both

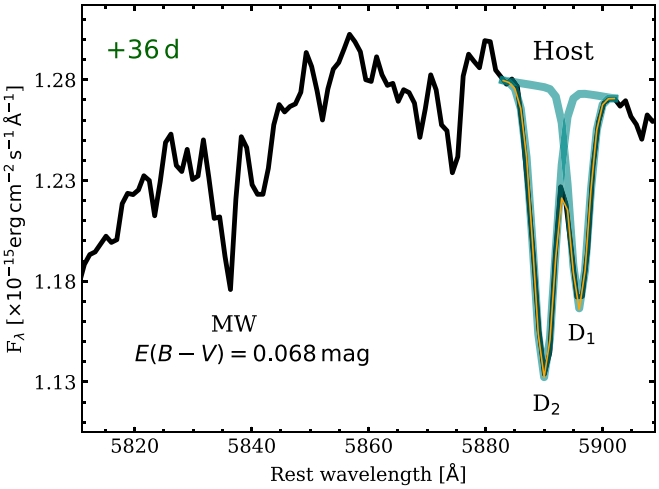

Figure 2. Zoom-in of the 5820–5900 Å region of the spectrum obtained on 2017 March 15 (36 days after explosion). Galactic DNa I and host absorption features are clearly visible. A multi-Gaussian fit (yellow line) of the marginally resolved host features including the single components (cyan lines). The spectrum is corrected for the recessional velocity of SN 2017ahn.

lines (see Figure 2). This ratio would suggest an additional contribution of $E(B - V) \simeq 0.18$ mag (assuming a standard extinction law) of the local environment to the total reddening. Because at this phase the feature is marginally resolved, we fit its profile using a combination of two Gaussians centered at the position of the D2 and D1 DNa I lines (see Figure 2). The fit gives parameters for both absorption features, including their EWs, resulting in ≃0.53 and ≃0.33 Å for D2 and D1, respectively. These are both within the linearity range of the relation between the sodium EW and dust extinction derived by Poznanski et al. (2012; see their Figure 9). Taking a weighted average between the quantities inferred using their Equations (7) and (8), these correspond to a contribution of $E(B - V) = 0.196 \pm 0.054$ mag to the total reddening. A similar result ($E(B - V) \simeq 0.12$ mag) is obtained using the relations found by Turatto et al. (2003, see also Blondin et al. 2009).

In order to avoid possible projection effects (SN 2017ahn lies at a projected distance of ≃160 pc from the center of the H II region, assuming a distance of 33 Mpc), we therefore favor $E(B - V) = 0.196$ mag as the contribution of the local environment to the total color excess in the direction of SN 2017ahn. This value has to be summed to the Galactic reddening in the direction of SN 2017ahn, resulting in a total extinction $E(B - V) = 0.264 \pm 0.054$ mag, although we cannot rule out a lower extinction value (see Section 4.3). In addition, as shown by Phillips et al. (2013), these relations largely underestimate errors on the derived values, and hence the uncertainty on the reddening is probably larger.

3. Evolution of the Main Observables

3.1. Light Curves

Optical and near-IR (NIR) light curves are shown in Figure 3, while the corresponding magnitudes and a description of the facilities used and reduction steps are reported in Appendix A.

The explosion epoch was estimated from the unfiltered light curve obtained with PROMPT5 (see the inset in Figure 3), taking the midpoint between the discovery (2017 February 8.29 UT; JD = 2457792.79) and the last nondetection limit

[23] https://cosmicflows.iap.fr
[24] http://edd.ifa.hawaii.edu/CF3calculator/
[25] ESO Programme ID 095.D-0172.

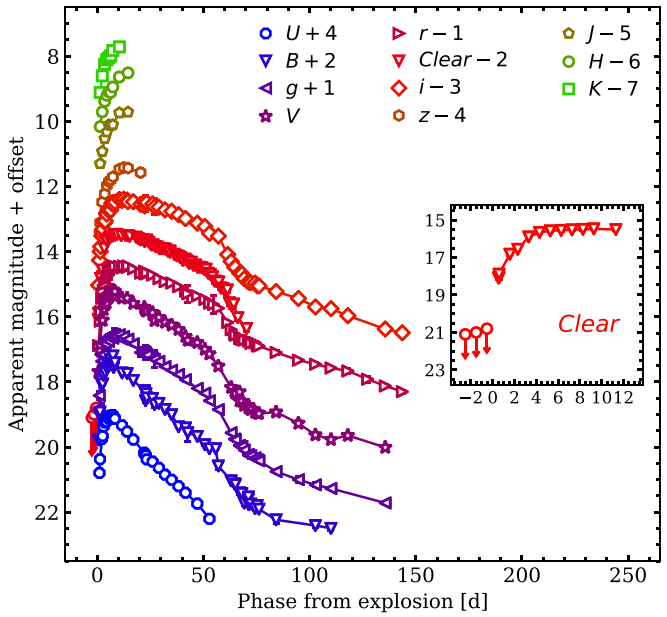

Figure 3. Optical and NIR light curves of SN 2017ahn. *U*, *B*, *V*, *Clear*, *J*, *H*, *K*, and *g*, *r*, *i*, *z* magnitudes were calibrated to the Vega and AB photometric systems, respectively. Magnitudes were not corrected for the foreground Galactic or host extinction. Phases refer to the estimated epoch of the explosion. In the inset, a zoom-in shows the last nondetection limits and the early evolution of the DLT40 data.

($m > 20.8$ mag on 2017 February 7.23 UT; JD = 2457791.73). In the following, we therefore assume 2017 February 7.76 UT (JD = 2457792.26 ± 0.5) as the explosion epoch for SN 2017ahn, and refer phases to this date.

Optical light curves show a relatively fast rise to maximum (see, e.g., Anderson et al. 2014b; Gall et al. 2015; González-Gaitán et al. 2015; Valenti et al. 2016) in all bands, with an average rate of ∼0.8 mag days^{-1}. Fitting high-order polynomials, we infer $t_{\rm rise} = t_{\rm max} - t_{\rm expl}$ ranging from 6.38 ± 0.66 days in *U* to 8.03 ± 0.71 days in *V*, with a similar behavior in *griz* (8.54 ± 2.24 days $\leqslant t_{\rm rise} \leqslant$ 14.04 ± 3.99 days). Errors were estimated by performing Monte Carlo simulations, for which we randomly shifted the photometric data within their uncertainties, including that on the estimated epoch of the explosion.

After peak, the light curves settle on a short plateau, lasting ≃50 days. This is more pronounced at redder wavelengths, except for the *U*−band, where the plateau declines linearly (with a rate of 0.069 ± 0.001 mag days^{-1}). At $t \gtrsim +70$ days, the optical light curves settle on a tail, with a slower decline at an average rate of ≃0.02 mag days^{-1}, with the exception of the *B*−band light curve, which shows a late decline of ≃0.01 mag days^{-1}. This suggests that the luminosity evolution is faster than that predicted by the radioactive ^{56}Co decay (see Section 4). Following Valenti et al. (2016), we infer a decline rate $s_{50,V} = 2.04 \pm 0.11$ mag 50 days^{-1} and a midpoint between the end of the plateau and the onset of the radioactive tail of $t_{{\rm pt},V} = 57.56 \pm 0.88$ days. These are similar to other fast-declining Type II SNe such as SNe 1980K, 2006Y (Anderson et al. 2014b), 2014G (Terreran et al. 2016), and 1998S (Fassia et al. 2000; see Figure 4).

In Figure 5 we compare the $B - V$ colors of SN 2017ahn to those of the sample of similarly fast-declining Type II SNe of Faran et al. (2014). The resulting evolution is consistent with the bluer end of the distribution, corresponding to colors similar to those shown by SNe 1999co and 1998S, which suggests a higher temperature for the pseudo-photosphere, as we discuss in the following sections. Following Patat et al. (1994), we identify two regimes with different slopes in the $B - V$ color evolution. Fitting linear relations, we find an initial evolution toward a redder color with a slope of 2.73 ± 0.06 mag 100 days^{-1}, followed by a slower evolution with a rate of 1.19 ± 0.09 mag 100 days^{-1}, in which a break occurs at $t_{\rm tr} \simeq +24.4$ days. These slopes are both steeper, and a break in the color evolution of SN 2017ahn occurs slightly earlier than the median values found for the sample of Type II SN of de Jaeger et al. (2018, $s_{1,(B-V)} \simeq 2.63$ and $s_{2,(B-V)} \simeq 0.77$ mag 100 days^{-1}, respectively, with $t_{\rm tr} \simeq 37.7$ days). At $t \gtrsim +75$ days we note a further flattening, in which the $B - V$ colors remain roughly constant throughout the remaining ≃25 days of photometric coverage.

Assuming the distance modulus and total reddening reported in Section 2, we infer absolute peak magnitudes ranging from $M_z = -17.81 \pm 0.29$ mag to $M_U = -19.08 \pm 0.29$ (with $M_V = -18.44 \pm 0.29$), where the errors are dominated by the uncertainty on the distance modulus and extinction (see Section 2).

A comparison with other transients showing similar photometric properties, based on the results reported above (see Figure 6), reveals an evolution of the absolute *V*-band magnitude similar to that of SN 1998S (Fassia et al. 2000; Liu et al. 2000), which despite the systematically brighter magnitudes and a slightly different rise time, shows the same relatively short plateau, with a comparable fast decline at $t \gtrsim +70$ days (0.002 ± 0.03 mag days^{-1}).

Given the similarities in the photometric evolution of SN 2017ahn and SN 1998S and the limited coverage of our NIR light curves, we cannot rule out an IR excess similar to the excesses that are typically observed in long-lasting Type IIn SNe (see, e.g., Gerardy et al. 2002; Fox et al. 2011) and in SN 1998S itself (see Pozzo et al. 2004). These features are often explained either as so-called light echoes by preexisting dust (see, e.g., Tartaglia et al. 2020) or as newly formed dust in the postshock regions (e.g., Smith et al. 2012). On the other hand, the absence of colder components in the NIR spectral continuum of SN 2017ahn seems to suggest a lack of a clear IR excess at least until +65 days (see Section 4).

The field of SN 2017ahn was also observed using the Ultraviolet/Optical Telescope (UVOT) on board the Neil Gehrels Swift Observatory (Gehrels et al. 2004), obtaining eight epochs that cover the early photometric evolution of SN 2017ahn (up to +15 days). The resulting light curves are shown in Figure 7, while details of the reduction steps are given in Appendix A. The light curves show a short and steep rise that is more pronounced at bluer wavelengths, where we measure an average increase in luminosity of ≃0.5 mag days^{-1} in *W*2, *M*2, and *W*1, respectively, that peaks at $t_{\rm max} \simeq +3.5$ days (*W*2, *M*2) and +5.3 days (*W*1). Rising UV light curves can either be interpreted as the simultaneous fast expansion and cooling of an extremely hot pseudo-photosphere ($T > 1.5 \times 10^4$ K) or as an intrinsic increase in UV luminosity and temperatures, such as the increases expected in the shocked regions of interacting transients. An upper limit on the X-ray counts was determined using aperture photometry through the HEAsoft packages (*xselect*; Blackburn 1995 and *xspec*; Arnaud 1996). The background was selected as a region outside the host galaxy without any known X-ray sources, and measured fluxes were converted from counts

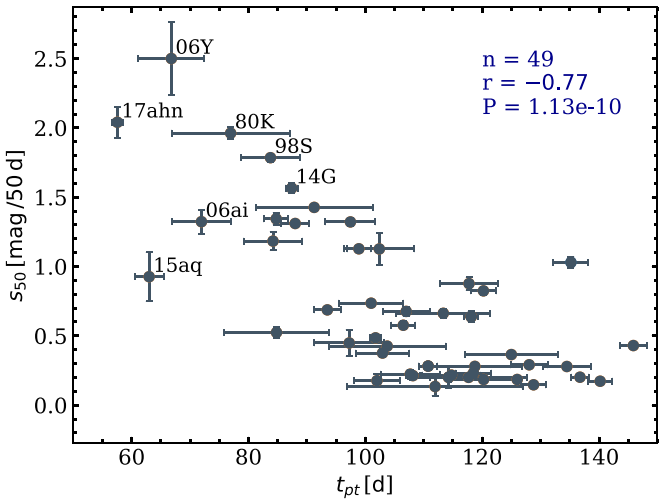

Figure 4. *V*-band decline rate measured at +50 days (s_{50}) vs. t_{pt} (see the main text) for the sample of Type II SNe of Valenti et al. (2016), including SN 2017ahn and SN 1998S. *n* is the number of objects in the sample, *r* the Pearson *s*−correlation coefficient, and *P* is the probability of obtaining a correlation by chance.

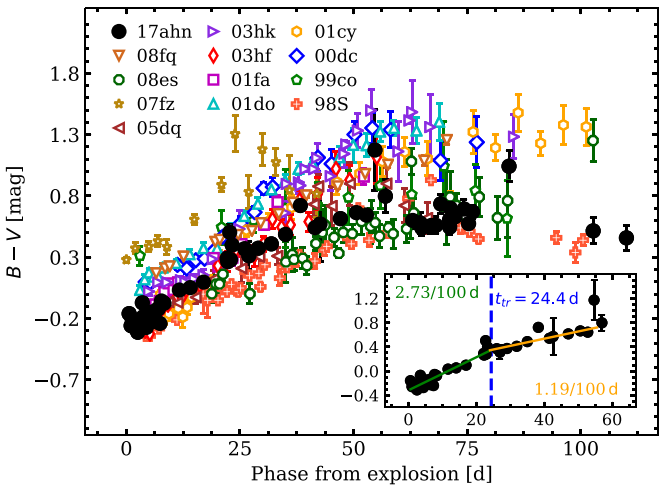

Figure 5. $B - V$ color curve of SN 2017ahn compared to the color evolution of the sample of Faran et al. (2014). The $B - V$ color evolution of SN 1998S is also included for comparison. Magnitudes were corrected for the total (Galactic +host) extinction.

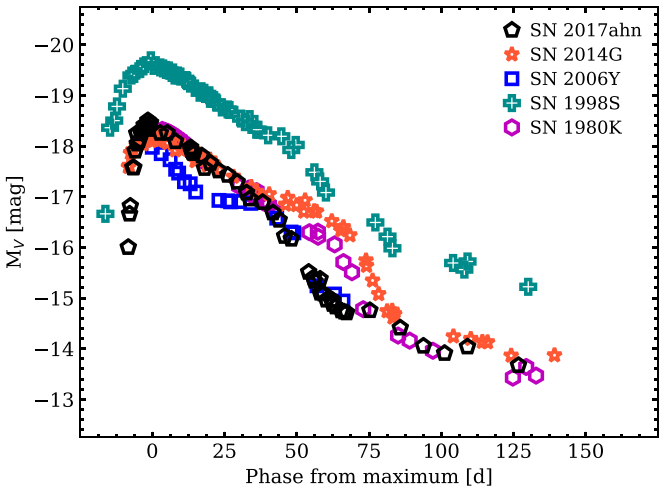

Figure 6. Absolute *V*-band light curve of SN 2017ahn compared to those of other transients showing a similar photometric evolution (see the main text).

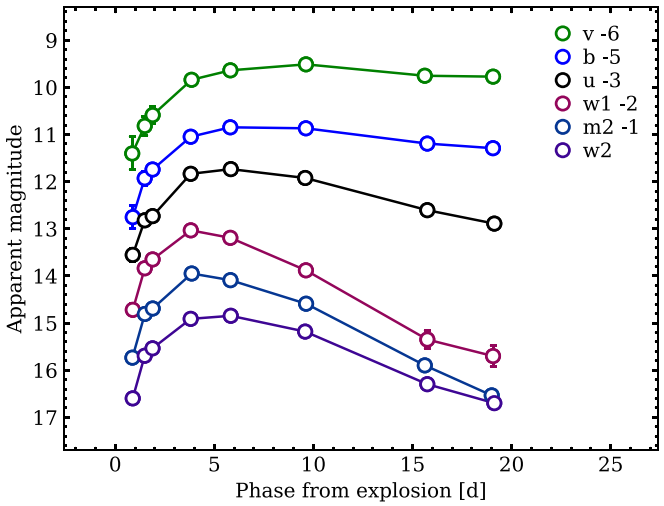

Figure 7. Swift UVOT light curves of SN 2017ahn. Magnitudes were calibrated to the Vega photometric system and have not been corrected for extinction.

per second into luminosities using PIMMS (Mukai 1993). No significant detections were found over an 18″ aperture by integrating over all available SWIFT/XRT epochs. This resulted in a limiting count rate of 0.904×10^{-3} counts s^{-1}, which, assuming a power-law model with a photon index of two and a Galactic absorption of 5.89×10^{20} cm^{-2} (Kalberla et al. 2005), corresponds to an unabsorbed flux of 3.25×10^{-14} erg cm^{-2} s^{-1} (0.3–10 keV) and a luminosity of 6.63×10^{39} erg s^{-1} at 33 Mpc.

3.2. Optical Spectra

Optical spectroscopy of SN 2017ahn was triggered soon after its discovery; the first spectrum was taken +1.7 days after explosion (although an earlier NIR spectrum was obtained at +1.4 days, see Section 3.3). The final spectra are shown in Figure 8, while the facilities we used and the reduction steps we employed are described in Appendix B.

Early spectra show a very blue continuum with prominent narrow lines in emission, along with strong DNa I lines at the redshift of the host galaxy. The DNa I features are usually related to a non-negligible reddening along the line of sight of the transient (see, e.g., Poznanski et al. 2012), and their EWs (0.53 and 0.33 Å for D2 and D1, respectively) suggest a moderately extinguished environment for SN 2017ahn (see Section 2). At +1.7 days and +2.1 days, the spectra show a number of narrow Balmer emission lines (Hα to Hδ), along with He II λ5411, C IV λ5801, N III, and N IV features. C IV and N IV features rapidly fade below the detection limit and are already no longer visible at +4.6 days, when He II λ5411 clearly emerges from the spectral continuum. High-ionization features (i.e., IVN III, C IV, and He II) become progressively fainter with time, although the signal-to-noise ratios (S/N) and resolutions of our spectra do not allow us to rule out the presence of these lines at later phases. At +6.1 days we also note the appearance of a narrow He I λ5875 feature that is not visible at later epochs.

The total integrated luminosity (after removing the contribution of the spectral continuum and assuming the reddening reported in Section 2) of the N III+He II feature shows an initial increase from $\simeq 1.4 \times 10^{40}$ erg s^{-1} to 1.6×10^{40} erg s^{-1} during the first +4.6 days, suggesting an increase in the production of

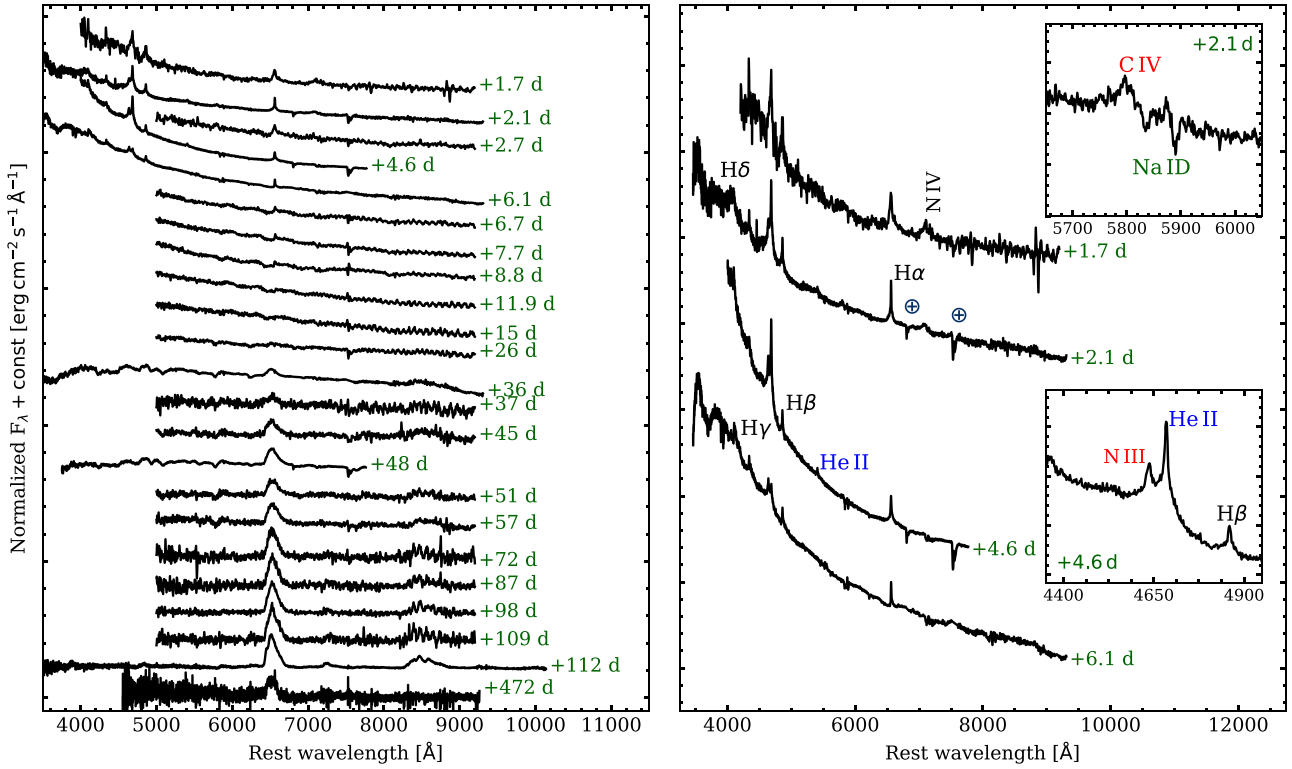

Figure 8. Left: optical spectra of SN 2017ahn. Spectra were corrected for the total reddening along the line of sight. Right: early spectroscopic evolution of SN 2017ahn. The spectrum at +1.7 days is rebinned to one-third of its original resolution to facilitate the visualization of the high-ionization features (see the main text). The most prominent features are identified. A crossed circle marks the position of the main telluric absorption features. Insets show zoom-in regions around DNa I (upper inset, including C IV λ5801) at +2.1 days and He II λ4686 (bottom inset, including N III) at +4.6 days. The spectra used to create this figure are available as Data behind the Figure.

(The data used to create this figure are available.)

ionizing photons in the underlying regions. We note the same evolution in the integrated luminosity of Hα, showing an increase in $\Delta L \simeq 1.2 \times 10^{38}$ erg s^{-1} over the same period, with a Hα/Hβ ratio evolving from $\simeq$0.4 (at +2.1 days) to $\simeq$1.9 (at +4.6 days). At +6.1 days the spectral shape shows the first significant signatures of evolution, with a drastic decrease in the integrated luminosity of the N III+He II feature ($\simeq 6.4 \times 10^{39}$ erg s^{-1}) and the Balmer emission lines (e.g., $L_{\mathrm{H}\alpha} \simeq 1.6 \times 10^{39}$ erg s^{-1}, with a Hα/Hβ ratio of $\simeq$1.7). We also note the appearance of broad and boxy absorption profiles in the blue part of the Balmer lines, with blue wings extending up to $\simeq 10^4$ km s^{-1}, corresponding to expansion velocities of the H-rich shell of $\simeq$6500 km s^{-1} (as derived from the minimum inferred through a Gaussian fit to the line profile).

At later epochs, the spectra show a further drastic change. The broad P Cygni profiles become progressively stronger (see Figure 9) and the spectral evolution resembles that of a typical Type II SN (see, e.g., Gutiérrez et al. 2017). At +36 days we clearly see broad Fe II (multiplet 42) and He I/DNa I features. At the same phases we also identify Sc II and a first hint of the presence of the NIR Ca II triplet, which remains relatively faint throughout the remaining spectroscopic evolution (see Figure 8), except for the +112 day spectrum, which is characterized by a significantly higher S/N at the corresponding wavelengths. At +112 days, we also note broad forbidden [O I] $\lambda\lambda$6300,6364 and [Ca II] lines that are typical of the nebular phases of Type II SNe, with an integrated luminosity of $\simeq 6.4 \times 10^{38}$ erg s^{-1} and $\simeq 2.3 \times 10^{39}$ erg s^{-1}, respectively. At +472 days the spectrum only shows a boxy, flat-topped Hα emission (see Figure 10), although the S/N does not allow us to rule out the presence of other nebular features at this epoch. Similarly, the S/N of the spectra at +51 days $\leqslant t \leqslant$ + 109 days does not allow us to rule out the appearance of a boxy profile at earlier phases, which would reveal the presence of different CSM layers.

Measuring the positions of the absorption minima at +36 days, we infer expansion velocities of $\simeq$5000 km s^{-1} from both Hβ and Fe II λ5169; the latter is usually considered a good proxy of the SN photospheric velocity (see, e.g., Dessart & Hillier 2005; Takáts & Vinkó 2012), although the complex structure of the spectral region around Hβ might suggest higher expansion velocities for the H-rich shell; see the inset in Figure 9. We infer similar values from the Sc II lines, while we do not note a significant evolution in the expansion velocities inferred at +36 and +48 days.

We obtained a rough estimate of the temperature evolution of the pseudo-photosphere by fitting a blackbody (BB) function to the spectral continuum, resulting in $T = 10{,}000 \pm 900$ K in both the +1.7-day and +2.1 -day spectra. At +4.6 days we note a drastic increase in the temperature ($\simeq$31,000 $\pm$ 5000 K) that is also reflected by the evolution of the spectral energy distribution (SED) inferred from photometry at the same epoch (see Section 4), followed by a progressive decrease to $\sim$5600 $\pm$ 600 K during the following $\sim$30 days. Although prominent Balmer lines (in particular Hα and Hβ) and high-ionization features can largely affect the shape of the

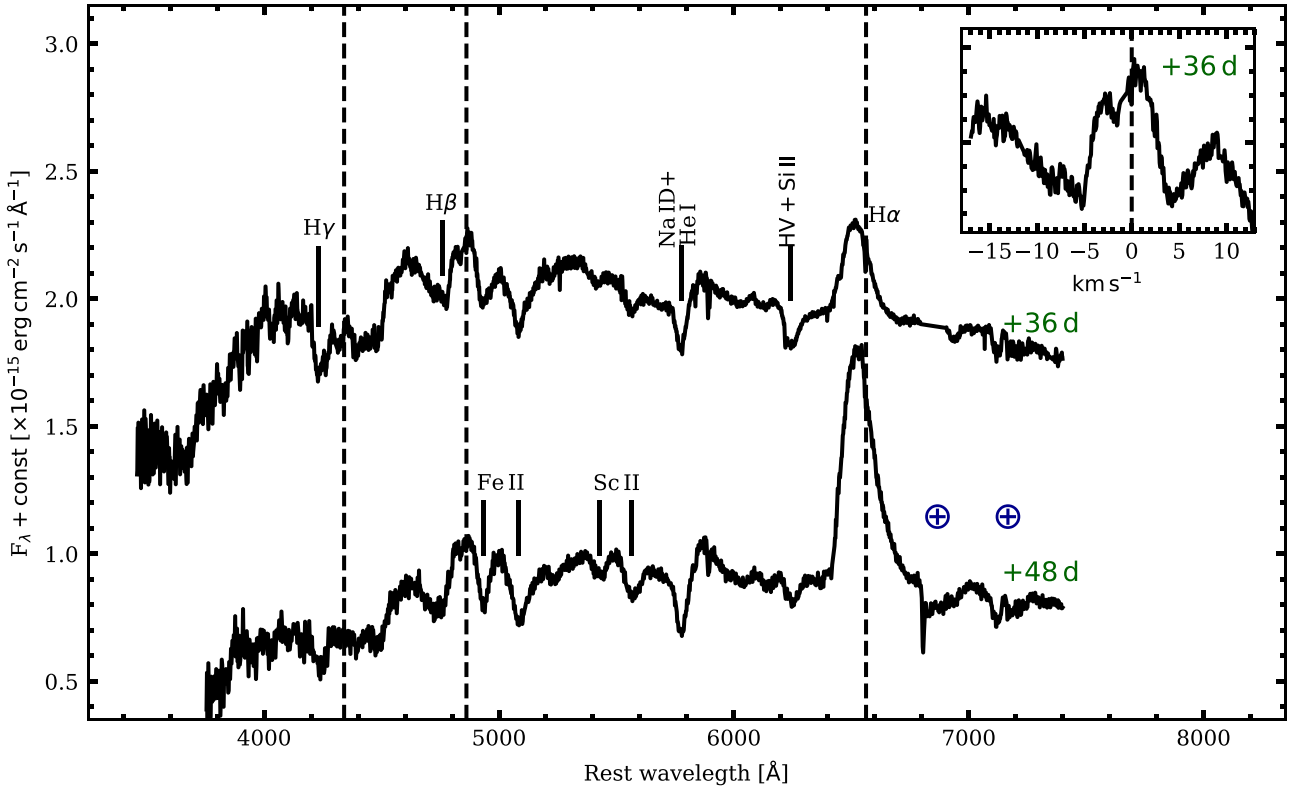

Figure 9. Identification of the main spectral features at +36 and +48 days. Dashed lines correspond to the rest wavelengths of the main Balmer lines, revealing the blueshift of the emission peaks that is typical of SNe II (Anderson et al. 2014a). The crossed circle marks the position of the residual telluric absorption features. A possible hydrogen high-velocity (HV) feature is also labeled (see the discussion in the main text). The inset shows a zoom-in of the Hβ region in the velocity space that presents the complex structure of the spectral region, with possible multiple absorption features centered at $\simeq -5000$ and $\simeq -10{,}000$ km s^{-1} with respect to the Hβ rest wavelength.

pseudo-continuum, we do not see a significant improvement in the fit, and we do not obtain different temperatures when regions dominated by narrow emission lines are exlcuded. On the other hand, the high temperatures inferred during the first 6.1 days suggest an SED that peaks at bluer wavelengths, which are not covered by the optical spectra. This in turn can significantly affect the proper determination of the temperature of the pseudo-continuum.

Balmer lines are visible throughout the spectroscopic evolution of SN 2017ahn. Up to +4.6 days, the most prominent H lines (i.e., Hα and Hβ) are purely in emission, with a slightly blueshifted peak ($V_{\rm shift} \simeq 70$ km s^{-1} that is probably due to a macroscopic velocity $V_{\rm bulk}$ of the recombining shell; see Fransson et al. 2014), that is characterized by narrow cores with an FWHM of $\simeq$300 km s^{-1} and by broader wings that extend up to a full width at zero intensity (FWZI) of $\simeq$4000 km s^{-1}. Similar velocities are also inferred from the profile of Hβ. While the overall profile might be contaminated by host lines (such as [N II] $\lambda\lambda$6548,6583), we note that the Hα line is not well reproduced using a single Gaussian or Lorentzian profile. This might either suggest the presence of recombining shells that move at different velocities or a broadening due to electron scattering in a dense ionized medium (see Section 4). At +6.1 days, the flux of the narrow Balmer lines decreases significantly (see above), and broad boxy absorption features appear in the blue part of Hα and Hβ. Interestingly, we infer different expansion velocities from the absorption minima of Hα and Hβ ($V_{\rm H\alpha} = 6500$ km s^{-1} versus $V_{\rm H\beta} = 1400$ km s^{-1}), suggesting an intrinsic difference in the expansion velocities of the absorbing shells. At $t \geqslant +36$ days, the Hα region (6100–6700 Å) is dominated by a broad, blueshifted, and boxy emission and a broad, boxy absorption component, with expansion velocities extending from $\simeq 1.2 \times 10^4$ to $\simeq 1.8 \times 10^4$ km s^{-1} with respect to the Hα rest wavelength, which becomes progressively fainter and disappears at $t \gtrsim$ 51 days. This can alternatively be identified as Si II λ6355, which would result in expansion velocities comparable to those derived from Fe II λ5169 (see Section 4). This interpretation is also supported by the overall shape of the emission component, which is symmetric with respect to its centroid and is well reproduced using a single Gaussian profile with an FWHM of $\simeq$5800 km s^{-1}. At the same epoch, Hα also shows a sharp P Cygni profile with a narrow emission component that peaks approximately at the line rest-wavelength, with an absorption component that extends up to 3×10^3 km s^{-1}, which is reminiscent of narrow features observed in sufficiently high-resolution spectra of Type IIn SNe (see, e.g., Fransson et al. 2014; Tartaglia et al. 2020). A more in-depth analysis also reveals an alternative decomposition, with Hα being the sum of a narrower component on top of a broader, flat-topped profile, also resulting in the presence of a blue shoulder, similar to that observed in SN 2013L (see, e.g., Figures 22 and 24 in Taddia et al. 2020) and other similar

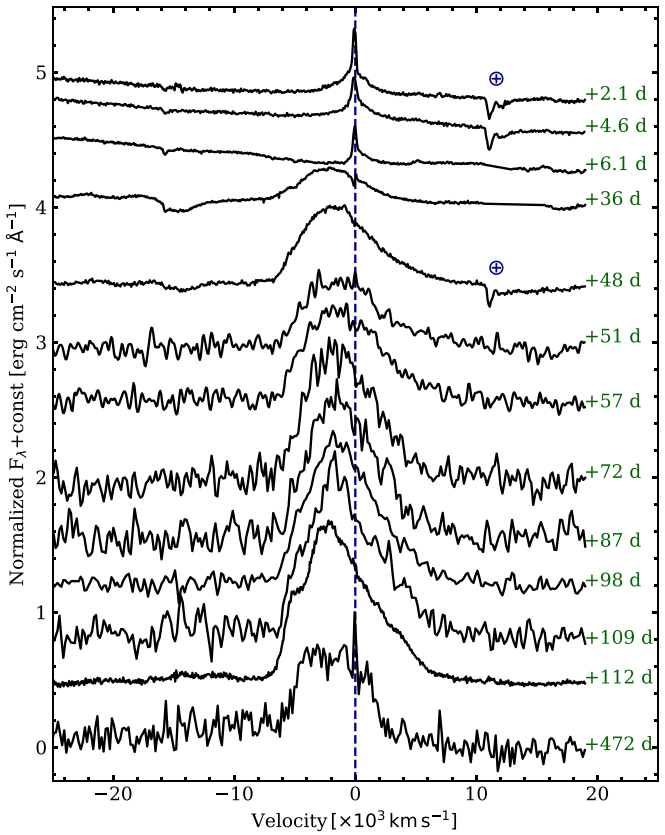

Figure 10. Evolution of the profile of Hα over the first 472 days of evolution of SN 2017ahn. Velocities were computed with respect to the Hα rest wavelength. The crossed circle marks the position of the main telluric absorption features, if visible. The spectrum at +472 days has been degraded to one-third of its resolution to facilitate the comparison.

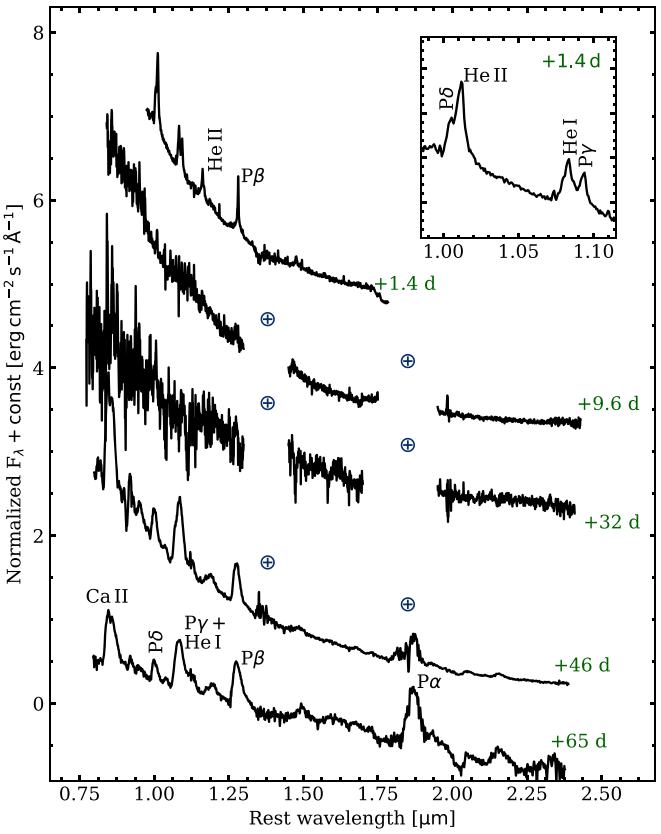

Figure 11. NIR spectra of SN 2017ahn. Spectra were corrected for the Galactic and host extinction, and wavelengths were corrected for redshift as inferred from the positions of the narrow DNa I galactic features. The crossed circles mark the positions of the most important telluric absorption features. The +65-day spectrum is shown in logarithmic scale in order to facilitate the comparison with earlier spectra. Spectra at +9.6 days and +32 days have been rebinned to one-third of their original resolutions to increase their S/N ratios. The inset shows a line identification in the blue part of the spectrum at +1.4 days. Spectra used to create this figure are available as Data behind the Figure.

(The data used to create this figure are available.)

interacting transients. This is also confirmed by the Hα profile at +472 days (see Figure 10).

3.3. Near-infrared Spectra

Near-IR spectroscopy of SN 2017ahn was triggered soon after discovery and resulted in a very early observation performed only 1.4 days after the estimated explosion epoch. To our knowledge, this is the earliest NIR spectrum of a Type II SN ever obtained. The complete NIR spectroscopic follow-up campaign spanned a period of ∼65 days, and the spectra are shown in Figure 11, while the reduction steps and information about the facilities we used are described in Appendix B.

At +1.4 days, the spectrum shows a blue continuum with prominent narrow Paschen (Paβ to Paδ) lines and He I (λ10830) and He II (λ10124 and λ11626) lines in emission, analogous to the flash features seen in the early optical spectra. At later times we note a spectroscopic evolution similar to that observed in the optical spectra, with a blue almost featureless continuum at both +9.6 and +32 days, with a progressive metamorphosis toward spectroscopic features typical of photospheric phases of Type II SNe. At +46 days, roughly corresponding to the endpoint of the plateau phase (see Section 3.1), we note broader Paschen lines (Paα to Paδ), along with Brβ and He I λ10830 features, which become stronger at +65 days (see Figure 11). At this epoch, He I clearly shows a P Cygni profile, with an absorption component extending up to 13,400 km s^{-1}, possibly consisting in a high-velocity (HV) component centered at −8650 km s^{-1}, with a redder component centered at −6300 km s^{-1} with respect to the He I rest wavelength. We note a similar structure also at +65 days, suggesting that this feature is real, although we cannot rule out the contribution of other lines such as Pγ and Sr II. If real, along with the measured EW ($\simeq$10 Å at +46 days), this would suggest a "weak" classification for SN 2017ahn when compared to the sample presented in Davis et al. (2019). On the other hand, given the lack of the blue notch in the He I emission component, which is attributed to Pγ+Sr II and typically observed in weak SNe, we favor the Pγ+Sr II identification for the blue feature, which in turn would suggest a "strong" classification for SN 2017ahn. This would also confirm the claim that fast-declining Type II SNe belong to the strong subclass (see Davis et al. 2019).

Isolated narrow lines at +1.4 days (i.e., Paβ and He II λ10124) are fairly well reproduced by a single Lorentzian profile, suggesting that the lack of broader electron-scattering wings is most likely due to the lower resolution compared to the +2.1-day and +4.6-day optical spectra (see Figure 8 and the description of optical spectra in Section 3.2). By $t = +9.6$ days, the Paβ integrated luminosity shows a decrease of $\Delta L = 3.3 \times 10^{38}$ erg s^{-1}, and the high-ionization He II lines also fade below the level of the spectral continuum. At

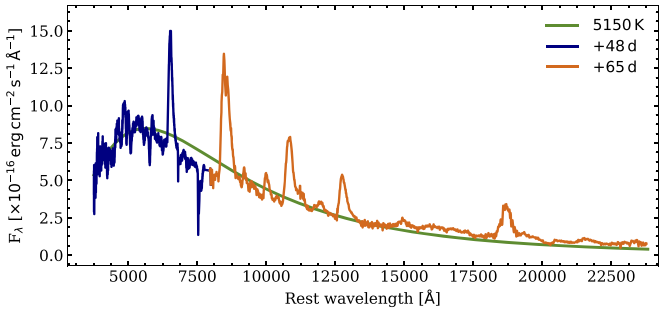

Figure 12. Combined optical+NIR spectra of SN 2017ahn at +48 days and +65 days. The spectral continuum is fairly well reproduced by a single BB (although it is affected by significant line-blanketing at $\lambda \lesssim 5000$ Å), ruling out the presence of a colder component at least until +65 days.

+46 days and +65 days, the Paschen lines show a slightly asymmetric profile, although they are still reasonably well reproduced by Gaussian profiles with an FWHM of $\simeq$6500 km s^{-1}.

Fitting a BB to the spectral continuum, we find an evolution similar to that observed in the optical spectra, although with slightly lower temperatures. Given the lack of NIR photometric data after peak and the similar spectroscopic evolution to that observed in SN 1998S, we investigate the possible presence of an IR excess by shifting the blue part of the NIR spectra at $t > +9.6$ days (i.e., the epochs missing a proper absolute flux calibration against photometry) in order to match the red parts of the optical spectra obtained at similar phases. In addition, we also compute synthetic *z*, *J*, *H*, *K* magnitudes from the derived spectra in order to have an estimate of the NIR part of the SED at these epochs (see Section 4). In Figure 12 we show the resulting optical+NIR spectrum obtained by combining the +48-day optical spectrum with the +65-day NIR spectrum. This clearly shows no evidence of a colder component, at least until +65 days.

4. Analysis and Discussion

In the following, we derive and discuss the main physical quantities obtained through simple modeling of the main observables described in the previous sections. In Sections 4.3 and 4.4 we also discuss the results of our numerical modeling of the early evolution of SN 2017ahn, and compare our results to those predicted by hydrodynamical models available in the literature.

4.1. Evolution of the Bolometric Luminosity

The evolution of the bolometric luminosity was estimated following the prescriptions of Tartaglia et al. (2020), including the contribution to the SED of the early UV bands at $t \lesssim 20$ days and extending the *z*, *J*, *H*, *K* light curves up to +65 days using synthetic magnitudes obtained from calibrated NIR spectra (see Section 3.3). The derived SEDs at each epoch were integrated using BBs without introducing any suppression factor at wavelengths bluer than $\sim$3000 Å (see, e.g., the discussion in Nicholl et al. 2017). This approach is based on a compromise between absorptions due to line blanketing (see, e.g., Pastorello et al. 2010; Chomiuk et al. 2011) and the UV flux excess predicted by synthetic spectra of Type IIn SNe (see, e.g., Figure 13 and the discussion in Dessart et al. 2015). Based on these considerations, the resulting evolution, shown in Figure 13, should still be considered a pseudo-bolometric light curve that

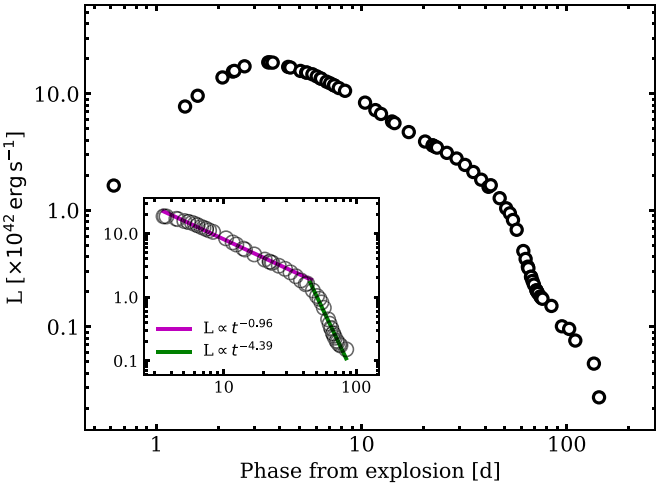

Figure 13. Evolution of the pseudo-bolometric luminosity of SN 2017ahn in logarithmic scale. The inset shows a zoom-in of the region between +3.5 days and +86 days that presents the broken power-la typical of interacting transients, with an initial evolution described by $L(t) \propto t^{-0.96}$ followed by a steeper decline described by $L(t) \propto t^{-4.39}$ with the break occurring at $t \simeq +45$ days.

possibly underestimates the actual luminosity of SN 2017ahn, in particular at early phases.

The bolometric light curve shows a fast rise lasting $\simeq$3.7 days with a peak luminosity of $\simeq 1.9 \times 10^{43}$ erg s^{-1} that rapidly declines to 2.5×10^{40} erg s^{-1} at $\sim$+144 days. The corresponding total radiated energy within the first $\sim$144 days is $\simeq 2.3 \times 10^{49}$ erg. At +3.5 days $\leqslant t \leqslant$ +86 days the luminosity evolution is well reproduced by a broken power law, a behavior typically observed in Type IIn SNe and other interacting transients (see, e.g., Fransson et al. 2014; Ofek et al. 2014; Tartaglia et al. 2020). We find that the bolometric light curve is well reproduced by $L(t) = 7.47 \times 10^{43}\, t^{-0.96}$ erg s^{-1} up to $\simeq$ +40 days, followed by a much steeper decline described by $L(t) = 3.1 \times 10^{49}\, t^{-4.39}$ erg s^{-1} up to $\sim$+86 days.

The late-time (i.e., during the post-plateau phases) bolometric light curve can be used to infer the mass of the radioactive ^{56}Ni expelled by the SN explosion. During the nebular phase, the bolometric light curves of SNe settle onto a radioactive tail, where the energy output is dominated by the ^{56}Co $\rightarrow$ ^{56}Fe decay. Assuming full γ-ray trapping (and hence a decline of $\simeq$1 mag 100 days^{-1}) within the opaque SN ejecta, it is therefore possible to obtain an estimate of the ejected ^{56}Ni mass through direct comparison of the late-time luminosity with that of SN 1987A at similar phases through the relation

$$M(^{56}\mathrm{Ni}) = 0.075 M_\odot \times \frac{L_{\mathrm{SN}}(t)}{L_{87A}(t)} \quad (1)$$

(see, e.g., Spiro et al. 2014, and references therein).

On the other hand, the late-time evolution of SN 2017ahn (see Figure 14) shows a much steeper decline than the one expected from the radioactive ^{56}Co decay. This is probably due to an incomplete trapping of the γ-rays produced in the radioactive decay. A similar evolution was also observed in the Type II-L SN 2014G, which also shows high-ionization features in early spectra. The evolution in this SN was attributed to an incomplete trapping of the γ-rays produced in the ^{56}Co decay (Terreran et al. 2016). Incomplete trapping has been discussed by Clocchiatti & Wheeler (1997), who found a simple relation to describe the late-time photometric evolution

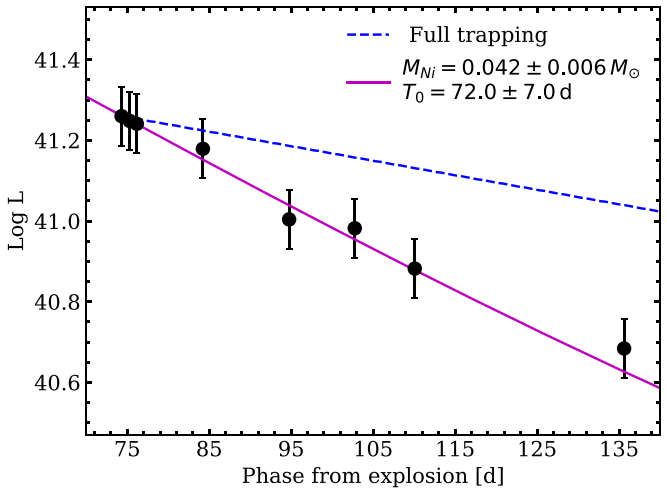

Figure 14. Fit of the modified radioactive decay model to the late-time bolometric light curve of SN 2017ahn. The full γ-ray trapping model is shown as a comparison.

for a sample of stripped envelope SNe,

$$L(t) = L_0(t) \times [1 - e^{-(T_0/t)^2}] \quad (2)$$

with T_0 the full-trapping characteristic timescale defined as

$$T_0 = \left(C\kappa_\gamma \frac{M_{\rm ej}^2}{E_k} \right)^{1/2}, \quad (3)$$

where $M_{\rm ej}$, E_k and k_γ are the total ejected mass, kinetic energy, and the γ-ray opacity and C a constant given by $C = (\eta - 3)^2[8\pi(\eta - 1)(\eta - 5)]$ for a density profile of the radioactive matter $\rho(r, t) \propto r^{-\eta}(t)$. The theoretical luminosity due to fully trapped ^{56}Co energy deposition is given by (see, e.g., Jerkstrand et al. 2012, and references therein)

$$L_0(t) = 9.92 \times 10^{41} \frac{M_{^{56}\rm Ni}}{0.07\, M_\odot} (e^{-t/111.4} - e^{-t/8.8}) \text{ erg s}^{-1}, \quad (4)$$

where $M_{^{56}\rm Ni}$ is the Ni mass expelled by the SN explosion. This model simply assumes spherical symmetry and homologous expansion of shells in which the entire radioactive matter is located at the center of the explosion.

Including Equation (4) in (2), we then fit the late-time bolometric light curve of SN 2017ahn to obtain a rough estimate of the ejected ^{56}Ni mass and the full-trap characteristic timescale, performing 10^4 Monte Carlo simulations for which we randomly shifted the luminosities within their errors. The resulting fit, giving $M_{^{56}\rm Ni} = 0.041 \pm 0.006\, M_\odot$ and $T_0 = 72 \pm 7$ days, is shown in Figure 14. This is consistent with the median value found by Anderson (2019) for a sample of Type II SNe ($0.032\, M_\odot$).

4.2. Shock-cooling Modeling of the Early Light Curves

Theoretical SN models predict that a short (seconds to hours) flash of X-ray/UV radiation is emitted when the radiation-mediated shock breaks through the stellar envelope, followed by UV/optical emission from the rapidly expanding and cooling layers. The analysis of the early post-break cooling phases can be used to infer crucial SN progenitor parameters, including its radius and surface chemical composition (see, e.g., Waxman & Katz 2017). In particular, the photospheric temperature and luminosity evolution during the early SN evolution can be described analytically as a function of the shock velocity, the opacity of the expanding medium, and the mass and radius of the progenitor star (see, e.g., Rabinak & Waxman 2011).

We model the early photometric evolution of SN 2017ahn in the context of early SN light curves that are dominated by shock-cooling radiation that escapes from the rapidly expanding progenitor envelope (see Sapir & Waxman 2017) using the same approach as adopted by Hosseinzadeh et al. (2018). They fit multiband light curves assuming $n = 3/2$ (the polytropic index for a typical RSG envelope) with a Markov chain Monte Carlo routine with flat priors for all parameters, 100 walkers, and 500 steps (see Hosseinzadeh 2020). The resulting fit (Figure 15) shows that the model fails to reproduce the early photometric evolution of SN 2017ahn, which seems to show faster rise times in the UV bands and brighter peaks, in particular in the bluer optical bands.

A plausible explanation must account for an additional source of energy, which in turn would affect the accuracy and validity of the Sapir & Waxman (2017) model. A similar explanation was given by Hosseinzadeh et al. (2018) to explain the fast early evolution of SN 2016bkv. Interaction with high-velocity SN ejecta and a dense preexisting medium, which is typically considered to power the light curves of narrow-line transients (e.g., SNe IIn; Schlegel 1990 and Ibn; Pastorello et al. 2016), can affect the overall shape of the light curve (both at early and late phases) and would require a different physical interpretation of the early SN phases. In stellar explosions that occur within a dense CSM, the SN shock is expected to break through the dense CSM that surrounds the progenitor star rather than the stellar envelope. This extends and diluted the SN radiation, with early light curves being dominated by photon diffusion rather than shock-cooling emission.

Although narrow lines are generally considered an indirect proof of ongoing interaction between expanding SN ejecta and a dense preexisting CSM, high-ionization features (C IV, N III, and N IV) are typically observed only at the very early phases (hours to a few days after explosion) and are thought to arise from the recombining CSM that is ionized by the shock breakout flash, rather than by photons emitted in shocked regions. On the other hand, in SN 2017ahn, such features disappear $\simeq$6 days after explosion, suggesting a simple scenario where the recombining CSM is progressively swept up by the rapidly expanding ejecta. Under specific conditions, an efficient conversion of kinetic energy into radiation would therefore be able to provide the required energy input to explain the early evolution of SN 2017ahn. This is also in agreement with the results obtained by Morozova et al. (2017, see also Morozova et al. 2018), who modeled the light curves of fast-declining Type II SNe. They suggested that red supergiants are surrounded by a dense CSM as viable progenitors and that the presence of this dense medium might be common among H-rich CC SNe. Although the pseudo-bolometric light curve of SN 2017ahn does not show the sudden drop at $t \simeq +25$ days predicted by the models of Moriya et al. (2011, corresponding to the dense shell becoming optically thin and the photosphere receding into the SN ejecta, see, e.g., their Figure 4), its overall shape is similar to their $10^{-3}\, M_\odot\, \text{yr}^{-1}$ model (see Sections 4.3 and 4.4).

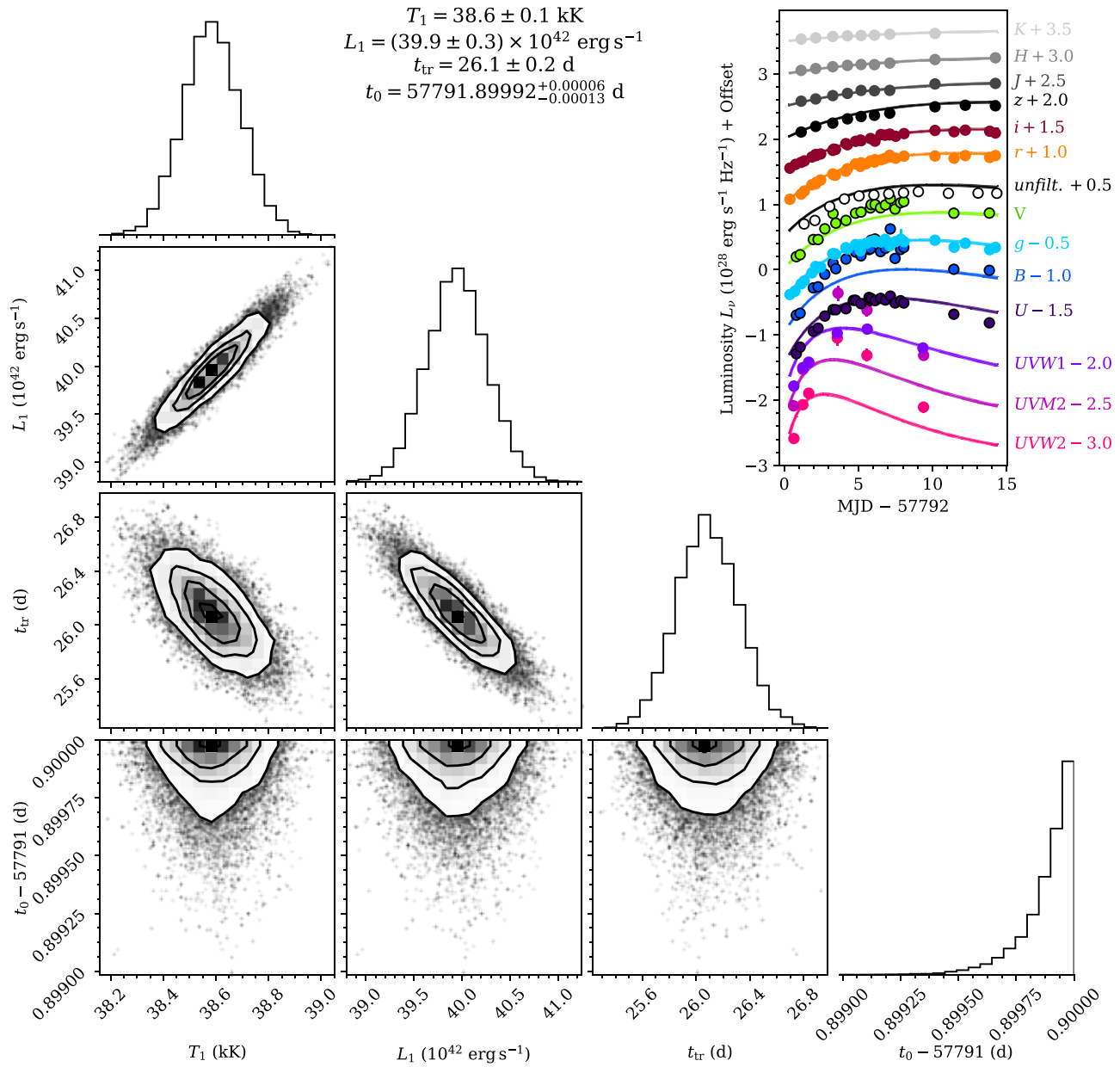

Figure 15. Posterior probability distributions and correlations between temperature (T1) and total luminosity (L1) at +1 days, the epoch at which the envelope becomes transparent (t_{tr}), and the discovery epoch (Δt_0) following the prescriptions of Hosseinzadeh et al. (2018). Shock-cooling models are not able to reproduce the early light curves of SN 2017ahn.

Interaction would also explain narrow Hα components with sharp P Cygni profiles at later times, which are observed up to +36 days, and the prominent boxy profile observed in the Hα profile at $t > +36$ days (Figure 10), showing a progressively asymmetric profile with a characteristic blueshifted ($V_{shift} \simeq 5000$ km s^{-1}) shoulder. Similar features are common among Type II SNe showing linearly declining light curves (see, e.g., the cases of SNe 1999ga Pastorello et al. 2009 and 2017ivv Gutiérrez et al. 2020 and the objects in the sample of Faran et al. 2014) as well as in a few Type IIn SNe at sufficiently late times (see, e.g., the cases of SNe 2005ip Stritzinger et al. 2012; Smith et al. 2017 and 2013L Taddia et al. 2020) and are typically considered evidence of emission from a shocked thick shell of gas (see, e.g., Jerkstrand 2017). Ongoing interaction of SN ejecta with a dense CSM at $t \gtrsim +6$ days (i.e., when high-ionization features seem to disappear) is also consistent with the radio nondetection of SN 2017ahn at 5.5 and 9 GHz (Ryder et al. 2017), suggesting efficient synchrotron self-absorption by free electrons in a dense medium at +21 days.

4.3. CMFGEN Models of the Early Interaction

To investigate the properties of SN 2017ahn at early times, we compute numerical models using the radiative-transfer code CMFGEN (Hillier & Miller 1998) with the implementation of Groh (2014). In our models, photons diffuse out through the extended material around the progenitor. Although we do not need to assume a source of energy, the photons are thought to be produced by the interaction between the SN ejecta and the progenitor wind. The wind heats up and emits continuum and line photons according to its temperature and density structure.

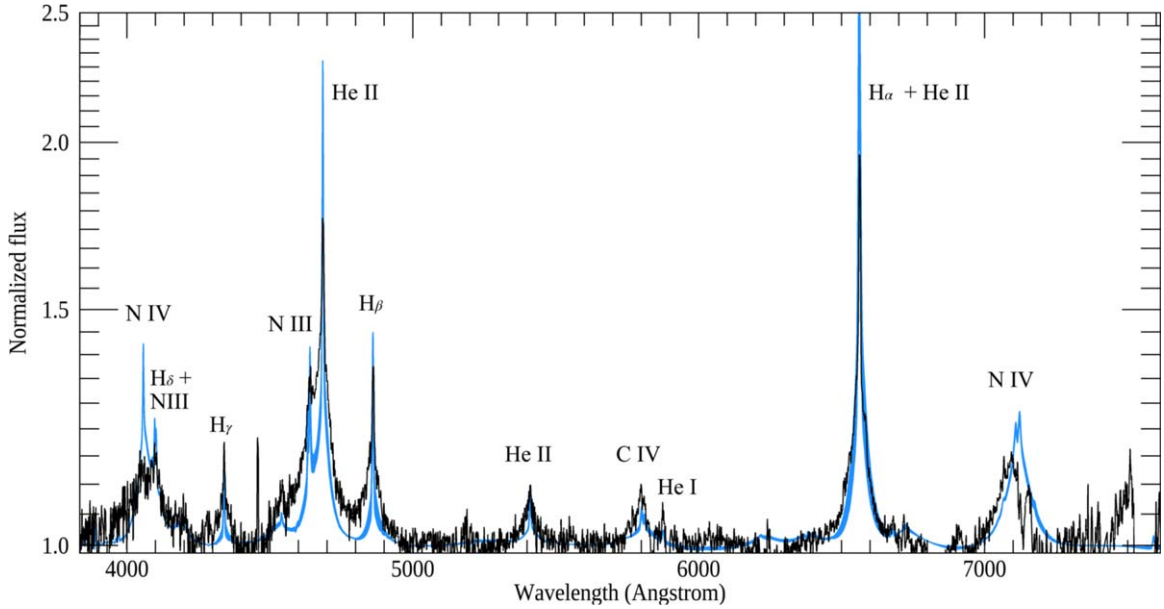

Figure 16. Best-fitting CMFGEN models (blue region) compared to the +2.1 days optical spectrum of SN 2017ahn. See Section 4.3 for our modeling technique and allowed range of parameters.

Our main assumptions are of a spherical and stationary wind, radiative equilibrium to compute the temperature structure, nonlocal thermodynamic equilibrium, and time-independent radiative transfer. The models take as input the luminosity of the event $L_{\rm SN}$, the progenitor mass-loss rate $\dot{M}$, wind terminal velocity υ_∞ and surface abundances, and the location of the inner boundary $R_{\rm in}$, which depends on the ejecta dynamics and time after explosion. Because the progenitor wind is dense, the photosphere is extended, and we quote two flux temperatures, $T_\star$ at the inner boundary (Rosseland optical depth of $\tau \simeq 10.0$), and $T_{\rm eff}$ at $\tau = 2/3$. We refer to Boian & Groh (2018, 2019, 2020) for further details.

We use the models presented in Boian & Groh (2020) as a starting point. These model grids were computed at 1.0, 1.8, and 3.8 days after explosion, exploring a wide range of parameters: $1.9 \times 10^8 \leqslant L \leqslant 2.5 \times 10^{10}\,L_\odot$, $5 \times 10^{-4} \leqslant \dot{M} \leqslant 10^{-2}\,M_\odot\,{\rm yr}^{-1}$, three values of chemical abundances (solar, He-rich, and CNO-processed), and fixed wind terminal velocities and ejecta expansion velocities of $\upsilon_\infty = 1.5 \times 10^2\,{\rm km\,s^{-1}}$ and $\upsilon_{\rm ej} = 10^4\,{\rm km\,s^{-1}}$, respectively. After we determined the best-fit models in the Boian & Groh (2020) grid, we computed 30 additional models in this region of parameter space to obtain the properties of SN 2017ahn at +2.1 days, corresponding to our highest S/N optical spectrum around that epoch. Figure 16 shows our best-fitting models compared with the observed spectrum.

We find that our CMFGEN models quantitatively reproduce the spectral morphology of SN 2017ahn at +2.1 days, with strong He II, H I, N III, and N IV features. Our models indicate $L = 5.0$–$7.2 \times 10^9\,L_\odot$, $\dot{M} = 2.7$–$4.0 \times 10^{-3}\,M_\odot\,{\rm yr}^{-1}$ (for $\upsilon_\infty = 150\,{\rm km\,s^{-1}}$), $R_{\rm in} = 2.17 \times 10^{13}$ cm, $T_\star = 26{,}600$–$28{,}900$ K, surface mass fractions $C_{\rm sur} = 5.6 \times 10^{-5}$, $N_{\rm sur} = 8.2 \times 10^{-3}$, and $O_{\rm sur} = 1.3 \times 10^{-4}$, with an estimated 3σ error of 50% and a He surface mass fraction of $Y \simeq 0.35$–0.50, suggesting some He enhancement, consistent with the scenario that the progenitor lost a significant fraction of its H envelope before exploding. Fitting the observed SED implies a total color excess of $E(B-V) = 0.06 \pm 0.01$ mag and $R_V = 3.1$, which, although it is in line with the extinction values found for a large sample of interacting SN (Boian & Groh 2020), is in contrast with the reddening derived from both the optical spectra (clearly showing strong DNa I features at all times; see Section 3.2) and the spectral analysis of the local environment (Section 2).

Our results show that the progenitor had CNO-processed surface abundances, with enhanced N and depleted C and O. The Geneva stellar evolution models suggest that this would be expected from a massive ($\sim$15–25 $M_\odot$) RSG, a yellow hypergiant, or a blue supergiant or luminous blue variable star (Groh et al. 2013). However, these models make strong assumptions about rotational mixing and mass loss, which have a key impact on the final CNO surface abundances (Meynet et al. 2013, 2015). In addition, a significant fraction of massive stars evolve in binary systems (Sana et al. 2012), with important consequences for the final mass and surface abundances. Finally, the final mass of red supergiants could be far higher than previously thought (Farrell et al. 2020a, 2020b). For all these reasons, it is challenging to map final surface abundances to progenitor initial or final masses (see also the discussion in Boian & Groh 2020).

We remark that the above quantities should be taken with caution given our model assumptions. In particular, an important role may also be played by asymmetries and/or particular geometrical configurations of the CSM, which were also believed to affect the evolution of the observables of SN 1998S (see Leonard et al. 2000) as well as CC SNe in general. We encourage further constraints on the CSM morphology of interacting SNe, which would allow these effects to be taken into account in future modeling of the early evolution of SN 2017ahn.

4.4. Comparison with Existing Hydrodynamic Models

After investigating our own models, we now compare the early photometric and spectroscopic evolution of SN 2017ahn with existing hydrodynamical models available in the literature. Dessart et al. (2017) used 1D radiation-hydrodynamics and 1D nonlocal thermodynamical equilibrium (LTE) radiative-transfer models to reproduce photometric and spectroscopic

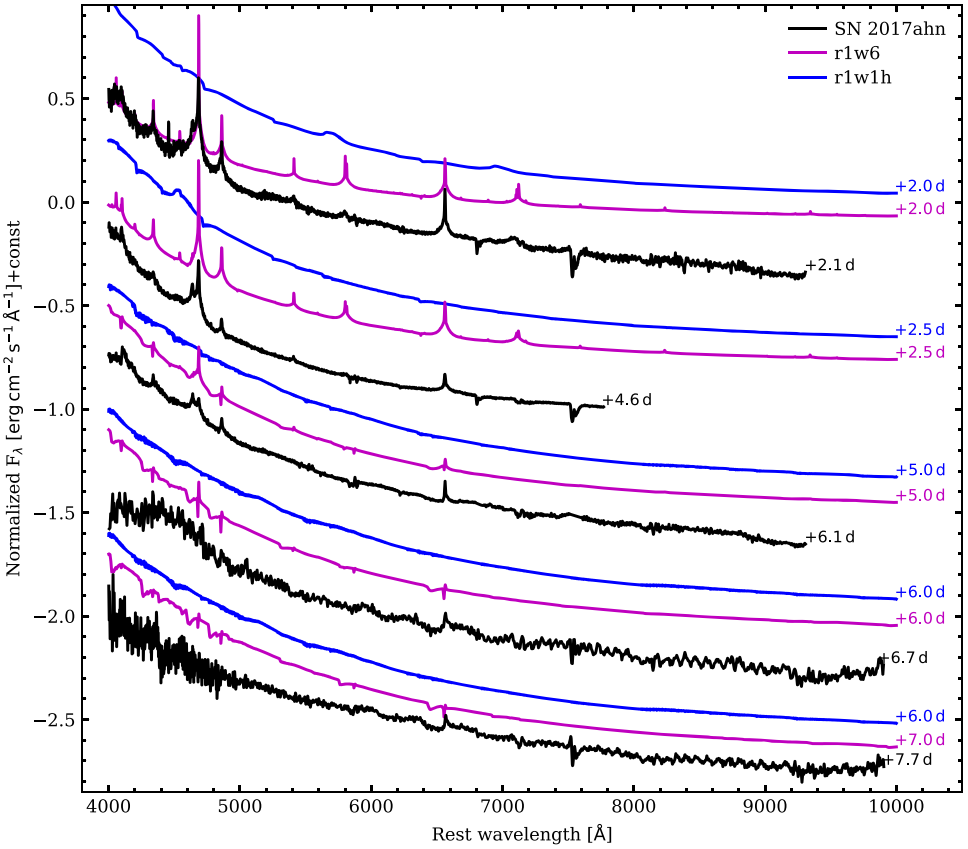

Figure 17. Comparison of the early ($t \lesssim 8$ days) spectra of SN 2017ahn, corrected for the total reddening reported in Section 2, with a selection of Dessart et al. (2017) models. Model r1w1h reproduces the shape of the continuum at all phases well, although it does not show emission features observed in the early spectra of SN 2017ahn. Model r1w6 is able to reproduce both the spectral continuum and most of the emission lines at $t > +2.5$ days, while at +2 days the overall spectral features are not reproduced well by any of the models presented in Dessart et al. (2017). These models were chosen because their evolutions are similar to that of SN 2017ahn, including the high-ionization features (e.g., Ne III, He II, and IVC III) at early phases, the shape of the continuum, and the timescale at which the spectra evolve (e.g., all other models have a much faster evolution; high-ionization features disappear a few hours after the shock breakout; see Figures C.1–C.7 in Dessart et al. 2017). These correspond to a progenitor radius $R_\star = 501\,R_\odot$, with mass-loss rates 10^{-6} (r1w1h), and to $10^{-2}\,M_\odot\,\mathrm{yr}^{-1}$ (r1w6, with $\dot{M} = 10^{-6}\,M_\odot\,\mathrm{yr}^{-1}$ beyond 5×10^{14} cm, see the main text and Dessart et al. (2017) for more details).

features of RSG stars that explode within moderately extended and massive winds, with $R_w \sim 10\,R_\star$ and a total mass $\lesssim 10\,M_\odot$. The resulting models were obtained using multigroup radiation-hydrodynamics simulations performed with HERACLES[26] (González et al. 2007) that were postprocessed using the radiative-transfer code CMFGEN[27] (Hillier & Miller 1998) with initial conditions described in Dessart et al. (2013, 2015). The result of a simple direct comparison of the observed early evolution of SN 2017ahn with their synthetic spectra is shown in Figure 17.

Although the evolution of the narrow spectral features is well matched by their r1w6 model, it fails to reproduce the shape of the blue spectral continuum, while the temperature of the pseudo-photosphere is well matched by model r1w1h, which, on the other hand, is not able to reproduce the evolution of the high-ionization features. These models both correspond to a RSG progenitor with $R_\star = 501\,R_\odot$, a total ejected mass of $12.52\,M_\odot$ with kinetic energy $E_k = 1.35 \times 10^{51}$ erg, colliding with a preexisting confined wind extending from 10^{15} to 2×10^{16} cm, a total mass of $2.89\,M_\odot$ (based on the mass of the CSM inferred by Fransson et al. 2014, for SN 2010jl), and an expansion velocity $u_w = 10^2\,\mathrm{km\,s^{-1}}$. The model r1w6, in particular, corresponds to a mass-loss rate of $10^{-2}\,M_\odot\,\mathrm{yr}^{-1}$ (10^{-6} beyond 5×10^{14} cm), while r1w1h assumes $\dot{M} = 10^{-6}\,M_\odot\,\mathrm{yr}^{-1}$ with a density scale height $H_\rho = 0.3R_\star$ followed by a power law with index 12 above $10^{-12}\,\mathrm{g\,cm^{-3}}$ ($H_\rho = 0.1R_\star$; see Dessart et al. 2017). Model r1w1h also seems to reproduce the shape of the pseudo-bolometric light curve of SN 2017ahn well (see Figure 18, where we compare it with the *uvoir* light curves[28] from Dessart et al. 2017), although with lower luminosities at all phases.

The main difference of r1w1 and r1w1h is the adopted value for the mass-loss rate (10^{-2} and $10^{-6}\,M_\odot\,\mathrm{yr}^{-1}$ for the dense and weak-wind models r1w6 and r1w1h, respectively), suggesting an intermediate value for SN 2017ahn. This is in agreement with our modeling discussed in Section 4.3, which gives a mass-loss rate of 2.7–4.0 $\times\ 10^{-3}\,M_\odot\,\mathrm{yr}^{-1}$. This idea is also supported by the mass-loss rate inferred by Shivvers et al. (2015) from their modeling of the spectra of SN 1998S, resulting in $\dot{M} = 6 \times 10^{-3}\,M_\odot\,\mathrm{yr}^{-1}$. On the other hand, we cannot rule out other explanations, as well as a combination of different parameters, including masses, velocities, and kinetic energies of the expanding SN ejecta and the preexisting CSM, or a different conversion rate of kinetic energy into radiation. Dessart et al. (2015) showed, for example, that a higher kinetic

[26] http://irfu.cea.fr/Projets/Site_heracles/
[27] http://kookaburra.phyast.pitt.edu/hillier/web/CMFGEN.htm
[28] Available at https://www-n.oca.eu/supernova/early/early.html.

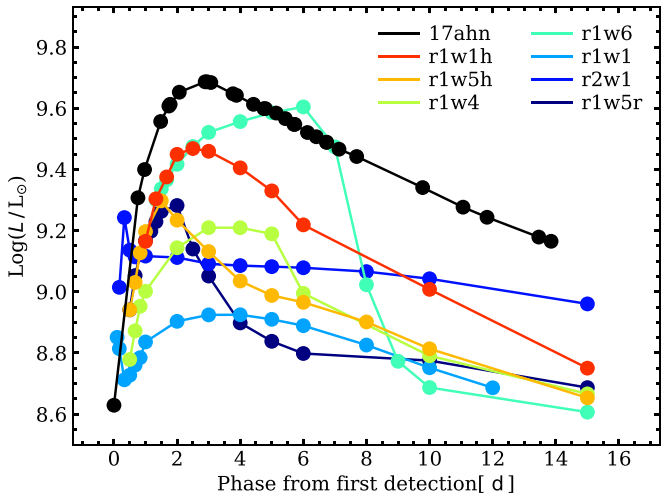

Figure 18. Comparison of the pseudo-bolometric light curve of SN 2017ahn with the *uvoir* models of Dessart et al. (2017). Model r1w1h, corresponding to a progenitor radius $R_\star = 501\,R_\odot$ with a mass-loss rate $\dot{M} = 10^{-6}\,M_\odot\,\mathrm{yr}^{-1}$ and an atmospheric density scale height $H_\rho = 0.1R_\star$ ($H_\rho = 0.3R_\star$ down to $\rho = 10^{-12}\,\mathrm{g\,cm}^{-3}$; see the main text and Dessart et al. 2017 for details) reproduces the shape of the light curve well, although with a slightly fainter luminosity at all phases.

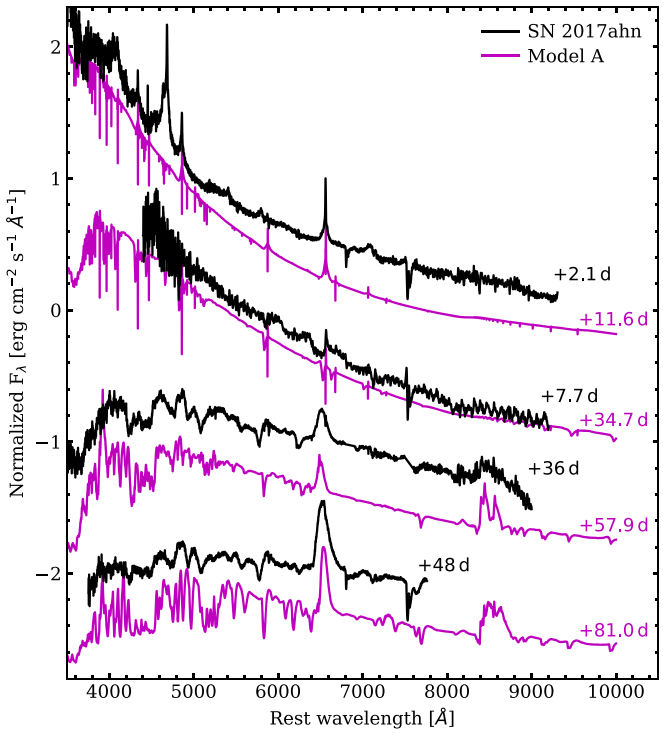

Figure 19. Comparison of the spectroscopic evolution of SN 2017ahn at selected epochs with Model A computed for SN 1998S in Dessart et al. (2016).

energy of the SN ejecta can give higher luminosities without affecting the overall shape of the light curve. Despite the limitations of our approach, the spectral and luminosity evolution predicted by models r1w6 and r1w1h agrees fairly well with the observed evolution of SN 2017ahn, considering these models were not specifically constructed on its observables.

Based on their similar spectroscopic evolutions, we also compare the spectroscopic evolution of SN 2017ahn with the radiative-transfer simulated spectra for SN 1998S presented in Dessart et al. (2016). Although the evolution of the narrow features seems to be slower (see Figure 19), Model A (see Figure 5 in Dessart et al. 2016) is able to reproduce the shape of the spectral continuum and the spectral features observed in SN 2017ahn well, although it fails to reproduce the N III+He II feature observed at $\leqslant$+6.1 days. This model, similar to that proposed by Chugai et al. (2004) for the Type IIn SN 1994W, corresponds to a massive ($M_{\rm ej} = 10\,M_\odot$) and energetic $E_k = 10^{51}$ erg shell that collides with a $0.4\,M_\odot$ dense CSM, produced by a stationary wind with a mass-loss rate of $0.1\,M_\odot\,\mathrm{yr}^{-1}$ with an expansion velocity of $10^2\,\mathrm{km\,s}^{-1}$ (see also Appendix A of Dessart et al. 2016, for more details about the model). These parameters contradict those inferred from simple comparison with other preexisting models (see above), highlighting the need of a more accurate modeling.

5. Summary and Conclusions

In this paper, we discussed the photometric and spectroscopic properties of the Type II SN 2017ahn, which was discovered soon after explosion by the DLT40 survey in the nearby galaxy NGC 3318. Multiwavelength follow-up campaigns, promptly activated after discovery, revealed a relatively fast early photometric evolution, showing peculiar fast-rising light curves in the UV bands that suggest a very high initial temperature of the pseudo-photosphere.

Like in SN 1998S, the early spectral evolution is characterized by prominent and narrow high-ionization features with narrow unresolved cores and broad wings. These are typical of electron-scattering profiles observed in Type IIn SNe, and are expected to be common during the very early phases of the evolution of CC SNe. These features become progressively fainter and disappear about a week after explosion, suggesting the presence of a confined dense shell that is progressively swept up by the expanding SN ejecta.

At later times, the evolution of SN 2017ahn resembles the evolutions that are typically observed in fast-declining Type II SNe, with a short plateau-like phase lasting $\sim$50 days, followed by a tail similar, although slightly steeper, to that predicted by the ^{56}Co radioactive decay during the nebular phases of SNe. According to Faran et al. (2014), the rapid decline rates observed in objects like SN 2017ahn both during the plateau and the nebular phases are consistent with those expected by fast-declining Type II SNe. Comparing the late evolution of the pseudo-bolometric light curve of SN 2017ahn to that of SN 1987A, we estimate an ejected ^{56}Ni mass of $0.041 \pm 0.006\,M_\odot$, with an incomplete trapping of the γ−rays produced in the radioactive Co decay, although this measurement could be affected by ongoing interaction of ejecta and CSM.

A non-negligible contribution of the interaction is also suggested by the evolution of the bolometric luminosity, which shows a broken power-law shape just before it settles on the radioactive tail, while Hα shows a late-time structured profile with a peculiar blue shoulder consistent with a boxy flat-topped emission component. In addition, the poor fit of the early light curves to shock-cooling models might also reveal a significant contribution of interaction to the total luminosity already at early times.

Numerical modeling of the early evolution of SN 2017ahn using the radiative-transfer CMFGEN (Hillier & Miller 1998) code suggests a massive (15–25 $M_\odot$) progenitor for SN 2017ahn, with a initial radius of $\simeq$310 $R_\odot$ and a mass-loss rate $\dot{M} = 2.7$–$4.0 \times 10^{-3}\,M_\odot\,\mathrm{yr}^{-1}$ (assuming $\upsilon_\infty = 1.5 \times 10^2\,\mathrm{km\,s}^{-1}$). A similar result was obtained through direct

comparison with existing non-LTE radiative-transfer models obtained with the HERACLES (González et al. 2007) and CMFGEN codes, suggesting a progenitor with a plausible mass-loss rate of $\simeq 3 \times 10^{-3}\,M_{\odot}\,\mathrm{yr}^{-1}$, although these models assume a less massive RSG progenitors (with an initial mass of $\simeq 14\,M_{\odot}$) and terminal velocity ($\upsilon_{\infty} = 50\,\mathrm{km\,s}^{-1}$, see Dessart et al. 2013, 2017). Although both approaches can give models that match many features observed in SN 2017ahn, they are unable to account for complex geometrical configurations, for the binarity of the progenitor system, and for their consequences on the final masses and surface abundances. Neither do they completely reproduce the early evolution of the observables, suggesting the need for continued modeling efforts. Nonetheless, the data and models support the idea that linearly declining Type II SNe arise from massive stars that are depleted of a significant fraction of their H-rich envelope in the pre-SN stage.

We gratefully acknowledge useful comments from N. Morrell.

Based on observations collected at The Gemini Observatory, under program GN-2016B-Q-57, which is operated by the Association of Universities for Research in Astronomy, Inc., under a cooperative agreement with the NSF on behalf of the Gemini partnership: the National Science Foundation (United States), the National Research Council (Canada), CONICYT (Chile), Ministerio de Ciencia, Tecnología e Innovación Productiva (Argentina), and Ministério da Ciência, Tecnologia e Inovação (Brazil).

VLT with MUSE, under the ESO programmes 095.D-0172 and 0101.D-0748.

The Magellan I Baade telescope at Las Campanas Observatory.

The SALT observations presented here were made through Rutgers University programs 2016-1-MLT-007 (PI: Jha); supernova research at Rutgers is supported by NSF award AST-1615455.

Part of the funding for GROND (both hardware and personnel) was generously granted from the Leibniz-Prize to Prof. G. Hasinger (DFG grant HA 1850/28-1).

This work makes use of observations from the Las Cumbres Observatory network of telescopes.

SNOoPy is a package for SN photometry using PSF fitting and/or template subtraction developed by E. Cappellaro. A package description can be found at http://sngroup.oapd.inaf.it/snoopy.html.

L.T. acknowledges support from MIUR (PRIN 2017 grant 20179ZF5KS).

Research by D.J.S. is supported by NSF grants AST-1821967, 1821987, 1813708, 1813466, 1908972, and by the Heising-Simons Foundation under grant #2020-1864. Research by S.V. is supported by NSF grants AST-1813176 and AST-2008108

J.S. acknowledges support from the Packard Foundation. R.C. and M.S. acknowledge support from STFC grant ST/L000679/1 and EU/FP7-ERC grant no [615929]. T.-W.C. acknowledges the EU Funding under Marie Skłodowska-Curie grant agreement No 842471. H.K. was funded by the Academy of Finland projects 324504 and 328898. D.A.H., J.B., and D.H. are supported by NSF grant AST-1911225 and NASA Swift grant 80NSSC19k1639. L.G. was funded by the European Union's Horizon 2020 research and innovation program under the Marie Skłodowska-Curie grant agreement No. 839090. This work has been partially supported by the Spanish grant PGC2018-095317-B-C21 within the European Funds for Regional Development (FEDER).

D.A.H., C.M., and G.H. are supported by NSF grant 1313484.

E.Y.H. acknowledges the support provided by the National Science Foundation under grant No. AST-1008343, AST-1613472 and AST-1613426.

This research has made use of the NASA/IPAC Extragalactic Database (NED), which is operated by the Jet Propulsion Laboratory, California Institute of Technology, under contract with the National Aeronautics and Space Administration.

SNOoPy is a package for SN photometry using PSF fitting and/or template subtraction developed by E. Cappellaro. A package description can be found at http://sngroup.oapd.inaf.it/ecsnoopy.html.

Facilities: Las Cumbres Observatory network of telescopes (Sinistro), FTN (FLOYDS), Swift (UVOT), VLT:Yepun (MUSE), SALT (RSS), IRTF (Spex), SOAR (Goodman), Gemini (FLAMINGOS-2), Magellan:BAADE (FIRE), MPG 2.2 m telescope (GROND).

Software: `astropy` (Astropy Collaboration et al. 2013; The Astropy Collaboration et al. 2018), `SNOoPY`: http://graspa.oapd.inaf.it/snoopy.html, `lpipe` (Perley 2019), `PySALT` (Crawford et al. 2010), FIREHOSE (Simcoe et al. 2013), LIGHTCURVE_FITTING (Hosseinzadeh 2020).

Appendix A
Photometric Data

PROMPT5 unfiltered DLT40 images were reduced as in Tartaglia et al. (2018), using our dedicated pipeline and calibrated to the *r* band. Magnitudes are reported in Table 1.

Optical photometry of SN 2017ahn was obtained mostly using the facilities of the Las Cumbres Observatory network (Brown et al. 2013) within the Supernova Key Project. Additional optical and NIR photometry was obtained, as part of the GREAT survey (Chen et al. 2018), using the Gamma-Ray Burst Optical/Near-Infrared Detector (GROND; Greiner et al. 2008), a seven-channel imager, collecting multicolor photometry in g', r', i', z' and *J*, *H*,

Table 1
DLT40 Unfiltered Light Curves of SN 2017ahn

Date	JD	Phase (days)	Open(err) (mag)
20170205	2457789.74	−2.52	>21.1
20170206	2457790.74	−1.52	>21.0
20170207	2457791.73	−0.53	>20.8
20170208	2457792.79	0.53	18.09(0.08)
20170208	2457792.84	0.58	18.07(0.08)
20170208	2457792.84	0.58	17.89(0.08)
20170209	2457793.84	1.58	16.82(0.06)
20170210	2457794.57	2.31	16.56(0.07)
20170211	2457795.56	3.30	15.90(0.05)
20170212	2457796.56	4.30	15.66(0.05)

Note. Magnitudes are calibrated to the *r* band. Data were obtained using the PROMPT5 0.41 m telescope at the Cerro Tololo Inter-American Observatory, Cerro Pachón, Chile. Phases refer to the epoch of the explosion.

(This table is available in its entirety in machine-readable form.)

Table 2
UBV Light Curves of SN 2017ahn

Date	JD	Phase (days)	*U*(err) (mag)	*B*(err) (mag)	*V*(err) (mag)	Instrument
20170208	2457792.87	0.61	⋯	17.89(0.04)	17.70(0.05)	1m0-09
20170208	2457793.32	1.06	16.83(0.06)	17.16(0.09)	17.04(0.08)	1m0-12
20170209	2457793.57	1.31	16.38(0.05)	17.03(0.05)	16.88(0.05)	1m0-09
20170209	2457794.46	2.20	15.79(0.05)	16.24(0.07)	16.11(0.09)	1m0-13
20170210	2457794.78	2.52	15.69(0.04)	16.16(0.05)	16.16(0.05)	1m0-09
20170210	2457795.24	2.98	15.40(0.08)	15.92(0.09)	15.77(0.10)	1m0-11
20170211	2457795.79	3.53	15.30(0.07)	15.72(0.22)	15.46(0.39)	1m0-05
20170211	2457795.98	3.72	15.30(0.08)	15.84(0.08)	15.64(0.09)	1m0-03
20170212	2457796.66	4.40	15.25(0.03)	15.67(0.04)	15.59(0.04)	1m0-09
20170212	2457797.16	4.90	15.10(0.20)	⋯	⋯	1m0-11

Note. Las Cumbres Observatory 1m0-03, 1m0-11: node at Siding Spring, Australia; 1m0-04, 0m4-05, 1m0-05, 1m0-09: node at Cerro Tololo Inter-American Observatory, Chile; 1m0-10, 1m0-12, 1m0-13: node at South African Astronomical Observatory, South Africa. Phases refer to the epoch of the explosion.

(This table is available in its entirety in machine-readable form.)

Table 3
griz Light Curves of SN 2017ahn

Date	JD	Phase (days)	*g*(err) (mag)	*r*(err) (mag)	*i*(err) (mag)	*z*(err) (mag)	Instrument
20170208	2457792.880	0.62	17.81(0.02)	17.88(0.04)	18.03(0.06)	⋯	1m0-09
20170208	2457793.220	0.96	17.42(0.14)	⋯	⋯	⋯	1m0-11
20170208	2457793.260	1.00	⋯	⋯	17.27(0.33)	⋯	0m4-03
20170209	2457793.640	1.38	16.87(0.02)	17.14(0.02)	17.00(0.02)	17.11(0.02)	GROND
20170209	2457793.855	1.59	16.71(0.04)	16.85(0.03)	16.85(0.04)	⋯	1m0-05
20170209	2457794.365	2.10	16.37(0.02)	16.43(0.02)	16.51(0.02)	⋯	1m0-13
20170210	2457794.620	2.36	16.15(0.06)	16.38(0.02)	16.34(0.02)	16.48(0.02)	GROND
20170210	2457794.657	2.40	16.21(0.04)	16.31(0.04)	16.41(0.04)	⋯	1m0-05
20170210	2457794.955	2.69	16.17(0.05)	16.19(0.05)	16.31(0.05)	⋯	1m0-11
20170211	2457795.770	3.51	15.82(0.02)	15.96(0.03)	16.11(0.02)	16.23(0.03)	GROND

Note. GROND: MPG 2.2 m telescope with GROND at the ESO La Silla Observatory, Chile; Las Cumbres Observatory 1m0-03, 1m0-11: node at Siding Spring, Australia; 1m0-04, 0m4-05, 1m0-05, 1m0-09: node at Cerro Tololo Inter-American Observatory, Chile; 1m0-10, 1m0-12, 1m0-13: node at South African Astronomical Observatory, South Africa. Phases refer to the epoch of the explosion. Table 3 is published in its entirety in machine-readable format. A portion is shown here for guidance regarding its form and content.

(This table is available in its entirety in machine-readable form.)

Table 4
UVOT Light Curves of SN 2017ahn

Date	JD	Phase (d)	*uvw*2(err) (mag)	*uvm*2(err) (mag)	*uvw*12(err) (mag)	*U*(err) (mag)	*B*(err) (mag)	*V*(err) (mag)
20170208	2457793.12	0.33	⋯	⋯	⋯	⋯	⋯	16.99(0.10)
20170208	2457793.13	0.34	⋯	16.65(0.06)	⋯	⋯	⋯	⋯
20170208	2457793.15	0.35	⋯	⋯	16.49(0.07)	⋯	⋯	⋯
20170208	2457793.15	0.35	⋯	⋯	⋯	16.43(0.06)	⋯	⋯
20170208	2457793.15	0.35	⋯	⋯	⋯	⋯	17.42(0.06)	⋯
20170208	2457793.15	0.36	16.62(0.08)	⋯	⋯	⋯	⋯	⋯
20170209	2457793.75	0.96	⋯	⋯	15.64(0.06)	⋯	⋯	⋯
20170209	2457793.75	0.96	⋯	⋯	⋯	⋯	16.76(0.05)	⋯
20170209	2457793.72	0.93	⋯	15.84(0.06)	⋯	⋯	⋯	⋯
20170209	2457793.75	0.96	⋯	⋯	⋯	⋯	⋯	16.58(0.07)

Note. Data were obtained using the 0.3 m UV/optical Telescope (UVOT) on board the Swift Gamma-Ray Burst Mission. Phases refer to the epoch of the explosion.

(This table is available in its entirety in machine-readable form.)

K_S bands simultaneously, mounted at the 2.2 m MPG telescope at ESO La Silla Observatory in Chile. These frames were prereduced using the dedicated GROND pipeline (Krühler et al. 2008), including bias and flat-field corrections, image stacking, and astrometric calibrations. Both optical and NIR magnitudes were obtained using the dedicated pipeline SNOOPY[29] and are listed in Tables 2–5.

[29] http://graspa.oapd.inaf.it/snoopy.html

Table 5
JHK Light Curves of SN 2017ahn

Date	JD	Phase (days)	*J*(err) (mag)	*H*(err) (mag)	*K*(err) (mag)
20170209	2457793.640	1.38	16.30(0.04)	16.16(0.04)	16.11(0.05)
20170210	2457794.620	2.36	15.93(0.05)	15.71(0.04)	15.61(0.05)
20170211	2457795.770	3.51	15.53(0.03)	15.39(0.06)	15.25(0.04)
20170212	2457796.760	4.50	15.33(0.05)	15.21(0.05)	15.11(0.05)
20170213	2457797.680	5.42	15.11(0.08)	15.10(0.04)	15.05(0.05)
20170214	2457798.580	6.32	15.13(0.04)	15.12(0.04)	14.99(0.04)
20170215	2457799.610	7.35	15.11(0.04)	14.95(0.05)	14.83(0.04)
20170218	2457802.660	10.40	14.74(0.04)	14.64(0.06)	14.72(0.04)
20170222	2457806.730	14.47	14.72(0.04)	14.51(0.06)	⋯

Note. Data were obtained using the MPG 2.2 m telescope with GROND, at the ESO La Silla Observatory, Chile. Phases refer to the epoch of the explosion.

Swift data were reduced using the pipeline of the Swift Optical Ultraviolet Supernova Archive (SOUSA; Brown et al. 2014), which is based on the method of Brown et al. (2009) using the zeropoints of Breeveld et al. (2011). The uncertainties account for differences in the measured brightness using a range of background regions with galaxy light similar to that of the SN. Magnitudes are reported in Table 4.

Appendix B
Spectroscopic Data

Optical spectra of SN 2017ahn were obtained using the facilities listed in Table 6. Most of the spectra were obtained using the Faulkes 2 m telescopes of the Las Cumbres Observatory network, located at the Haleakala Observatories (Faulkes Telescope North, Hawaii—U.S.; FTN) and the Siding Spring Observatory (Faulkes Telescope South, Australia; FTS) using the cross-dispersed, low-resolution spectrographs FLOYDS and reduced using their dedicated pipeline[30] (Valenti et al. 2014). Optical spectra were also obtained using the 10 m Southern African Large Telescope (SALT), located at the South African Astronomical Observatory (SAAO), Sutherland, South Africa, with the Robert Stobie Spectrograph (RSS; reduced using the dedicate pipeline PYSALT; Crawford et al. 2010) and the 4.1 m SOuthern Astrophysical Research telescope (SOAR) with the Goodman High Throughput Spectrograph (Clemens et al. 2004), located at the Cerro Tololo Inter-American Observatory, Cerro Pachón, Chile, and reduced using a dedicated pipeline.[31] One additional optical spectrum was obtained using the 10 m Keck I telescope located at the Maunakea Observatories (Hawaii, U.S.) using the Low Resolution Imaging Spectrometer (LRIS; Oke et al. 1995; Rockosi et al. 2010) and reduced using the automated pipeline LPIPE[32] (Perley 2019). MUSE data reduction was performed using the ESO MUSE data reduction pipeline under the Reflex interface (Freudling et al. 2013), which includes bias subtraction, flat-fielding, wavelength and flux calibrations, background sky subtraction, and atmospheric effects correction. The spectra were subsequently extracted from the reduced MUSE data cube for further analysis.

Near-infrared spectra were taken with the FLAMINGOS-2 instrument (F2; Eikenberry et al. 2006) at the Gemini South Observatory, SpeX instrument (Rayner et al. 2003) on the NASA Infrared Telescope Facility and the Folded-port InfraRed Echellette instrument (FIRE; Simcoe et al. 2013) on the Magellan Baade telescope. The IRTF SpeX data were taken in cross-dispersed SXD mode with the $0\farcs5$ slit, yielding a wavelength coverage from $\sim$0.7 to 2.4 μm and a $R \sim 1200$. The Magellan FIRE spectra were obtained in high-throughput prism mode with a $0\farcs6$ slit, giving continuous wavelength coverage from 0.8 to 2.5 μm. For the Gemini South F2 spectra, we observed with the JH grism and $0\farcs72$ slit in place, yielding a wavelength range of 1.0–1.8 μm. All observations were taken with a standard ABBA pattern for sky subtraction, and an A0V star was observed adjacent to the science exposures for both telluric corrections and flux calibration. Data for both instruments were reduced in a standard way as described in Hsiao et al. (2019), and we refer to Hsiao et al. for the details.

[30] https://lco.global/documentation/data/floyds-pipeline/
[31] http://www.ctio.noao.edu/soar/content/goodman-data-reduction-pipeline
[32] https://www.astro.caltech.edu/~dperley/programs/lpipe.html

Table 6
Log of the Spectroscopic Observations of SN 2017ahn

Date	JD	Phase (d)	Instrumental Setup	Grism/Grating	Spectral Range (Å)	Exposure Time (s)	Resolution (Å)
20170209	2457793.70	+1.4	GeminiS+FLAMINGOS2	JH	10000–18000	2400	14.0
20170209	2457793.97	+1.7	FTN+FLOYDS	235 l/mm	3500–9000	3600	15.0
20170209	2457794.37	+2.1	SALT+RSS	PG0900	3500–9000	2500	5.6
20170210	2457794.96	+2.7	FTS+FLOYDS	235 l/mm	5000–10000	3600	14.3
20170212	2457796.82	+4.6	SOAR+GOODMAN	SYZY_400	3500–8000	900	6.5
20170213	2457798.35	+6.1	SALT+RSS	PG0900	3500–9000	2600	5.6
20170214	2457798.97	+6.7	FTS+FLOYDS	235 l/mm	5000–10000	3600	16.9
20170215	2457799.92	+7.7	FTS+FLOYDS	235 l/mm	5000–10000	3600	17.0
20170216	2457801.10	+8.8	FTS+FLOYDS	235 l/mm	5000–10000	3600	17.2
20170217	2457801.91	+9.6	IRTF+Spex	ShortXD	8000–24000	2400	11.7
20170219	2457804.19	+11.9	FTS+FLOYDS	235 l/mm	5000–10000	3600	19.0
20170222	2457807.24	+15	FTS+FLOYDS	235 l/mm	5000–10000	3600	17.7
20170305	2457817.91	+26	FTN+FLOYDS	235 l/mm	5000–10000	3600	14.8
20170311	2457823.89	+32	IRTF+Spex	ShortXD	8000–24000	3000	11.7
20170315	2457828.53	+36	SALT+RSS	PG0900	3500–9000	2230	5.6
20170316	2457828.90	+37	FTN+FLOYDS	235 l/mm	5000–9000	3600	16.5
20170324	2457836.83	+45	FTN+FLOYDS	235 l/mm	5000–9000	3600	15.8
20170326	2457838.69	+46	Baade+FIRE	LDPrism	8500–24000	2282	24.0
20170327	2457840.48	+48	SOAR+GOODMAN	SYZY_400	3500–8000	900	5.7
20170330	2457842.92	+51	FTS+FLOYDS	235 l/mm	5000–9000	3600	19.0
20170405	2457848.80	+57	FTN+FLOYDS	235 l/mm	5000–9000	3600	14.9
20170414	2457857.69	+65	Baade+FIRE	LDPrism	8500–24000	2028	24.0
20170420	2457864.00	+72	FTS+FLOYDS	235 l/mm	5000–9000	3600	19.3
20170505	2457879.01	+87	FTS+FLOYDS	235 l/mm	5000–9000	3600	18.7
20170516	2457889.94	+98	FTS+FLOYDS	235 l/mm	5000–9000	3600	19.8
20170527	2457900.86	+109	FTS+FLOYDS	235 l/mm	5000–9000	3600	19.8
20170530	2457903.77	+112	KECK+LRIS	600/4000+400/8500	3500–10000	180 + 180	6.5
20180526	2458264.63	+472	VLT+MUSE	VPH	4600–9200	4 × 600	3.0

Note. FTN: 2 m Faulkes Telescope North, Las Cumbres Observatory node at the Haleakala Observatory, Hawaii; FTS: 2 m Faulkes Telescope South, Las Cumbres Observatory node at the Siding Spring Observatory, Australia; SALT: 10 m Southern Africa Large Telescope at the South African Astronomical Observatory (SAAO), Sutherland, South Africa; SOAR: SOuthern Astrophysical Research telescope and GeminiS: 8 m Gemini South telescope, both at the Cerro Tololo Inter-American Observatory, Cerro Pachón, Chile; BAADE: m Magellan 1—Baade Telescope located at the Las Campanas Observatory of the Carnegie Institution for Science, Cerro Las Campanas, Chile; KECK: 10 m Keck I telescope, at the Maunakea Observatory, Hawaii—U.S. MUSE: 8.2 m Very Large Telescope, European Southern Observatory, Cerro Paranal, Chile.

ORCID iDs

L. Tartaglia https://orcid.org/0000-0003-3433-1492
D. J. Sand https://orcid.org/0000-0003-4102-380X
J. H. Groh https://orcid.org/0000-0001-7675-3381
S. Valenti https://orcid.org/0000-0001-8818-0795
S. D. Wyatt https://orcid.org/0000-0003-2732-4956
K. A. Bostroem https://orcid.org/0000-0002-4924-444X
P. J. Brown https://orcid.org/0000-0001-6272-5507
S. Yang https://orcid.org/0000-0002-2898-6532
T.-W. Chen https://orcid.org/0000-0003-1532-0149
S. Davis https://orcid.org/0000-0002-2806-5821
F. Förster https://orcid.org/0000-0003-3459-2270
L. Galbany https://orcid.org/0000-0002-1296-6887
D. Hiramatsu https://orcid.org/0000-0002-1125-9187
G. Hosseinzadeh https://orcid.org/0000-0002-0832-2974
D. A. Howell https://orcid.org/0000-0003-4253-656X
E. Y. Hsiao https://orcid.org/0000-0003-1039-2928
S. W. Jha https://orcid.org/0000-0001-8738-6011
V. Kouprianov https://orcid.org/0000-0003-3642-5484
H. Kuncarayakti https://orcid.org/0000-0002-1132-1366
C. McCully https://orcid.org/0000-0001-5807-7893
M. M. Phillips https://orcid.org/0000-0003-2734-0796
A. Rau https://orcid.org/0000-0001-5990-6243
D. E. Reichart https://orcid.org/0000-0002-5060-3673
M. Shahbandeh https://orcid.org/0000-0002-9301-5302
J. Strader https://orcid.org/0000-0002-1468-9668

References

Anderson, J. P. 2019, A&A, 628, A7
Anderson, J. P., Dessart, L., Gutierrez, C. P., et al. 2014a, MNRAS, 441, 671
Anderson, J. P., González-Gaitán, S., Hamuy, M., et al. 2014b, ApJ, 786, 67
Anderson, J. P., Habergham, S. M., James, P. A., & Hamuy, M. 2012, MNRAS, 424, 1372
Arnaud, K. A. 1996, in ASP Conf. Ser. 101, Astronomical Data Analysis Software and Systems V, ed. G. H. Jacoby & J. Barnes (San Francisco, CA: ASP), 17
Astropy Collaboration, Robitaille, T. P., Tollerud, E. J., et al. 2013, A&A, 558, A33
Bacon, R., Vernet, J., Borisova, E., et al. 2014, Msngr, 157, 13
Balberg, S., & Loeb, A. 2011, MNRAS, 414, 1715
Barbon, R., Ciatti, F., & Rosino, L. 1979, A&A, 72, 287
Bellm, E. C., Kulkarni, S. R., Graham, M. J., et al. 2019, PASP, 131, 018002
Blackburn, J. K. 1995, in ASP Conf. Ser. 77, Astronomical Data Analysis Software and Systems IV, ed. R. A. Shaw, H. E. Payne, & J. J. E. Hayes (San Francisco, CA: ASP), 367
Blinnikov, S. I., & Bartunov, O. S. 1993, A&A, 273, 106
Blondin, S., Prieto, J. L., Patat, F., et al. 2009, ApJ, 693, 207
Boian, I., & Groh, J. H. 2018, A&A, 617, A115
Boian, I., & Groh, J. H. 2019, A&A, 621, A109
Boian, I., & Groh, J. H. 2020, MNRAS, 496, 1325
Breeveld, A. A., Landsman, W., Holland, S. T., et al. 2011, in AIP Conf. Ser. 1358, Gamma Ray Bursts 2010, ed. J. E. McEnery, J. L. Racusin, & N. Gehrels (Melville, NY: AIP), 373

Brown, P. J., Breeveld, A. A., Holland, S., Kuin, P., & Pritchard, T. 2014, Ap&SS, 354, 89
Brown, P. J., Holland, S. T., Immler, S., et al. 2009, AJ, 137, 4517
Brown, T. M., Baliber, N., Bianco, F. B., et al. 2013, PASP, 125, 1031
Cardelli, J. A., Clayton, G. C., & Mathis, J. S. 1989, ApJ, 345, 245
Carrick, J., Turnbull, S. J., Lavaux, G., et al. 2015, MNRAS, 450, 317
Chassagne, R., Maury, A., Vanzi, L., Testi, L., & Lidman, C. 2000, IAUC, 7432, 1
Chen, T. W., Inserra, C., Fraser, M., et al. 2018, ApJL, 867, L31
Chevalier, R. A. 1982, ApJ, 258, 790
Chevalier, R. A., & Fransson, C. 1994, ApJ, 420, 268
Chomiuk, L., Chornock, R., Soderberg, A. M., et al. 2011, ApJ, 743, 114
Chugai, N. N., Blinnikov, S. I., Cumming, R. J., et al. 2004, MNRAS, 352, 1213
Clemens, J. C., Crain, J. A., & Anderson, R. 2004, Proc. SPIE, 5492, 331
Clocchiatti, A., & Wheeler, J. C. 1997, ApJ, 491, 375
Courtois, H. M., & Tully, R. B. 2012a, AN, 333, 436
Courtois, H. M., & Tully, R. B. 2012b, ApJ, 749, 174
Crawford, S. M., Still, M., Schellart, P., et al. 2010, Proc. SPIE, 7737, 773725
Davis, S., Hsiao, E. Y., Ashall, C., et al. 2019, ApJ, 887, 4
de Jaeger, T., Anderson, J. P., Galbany, L., et al. 2018, MNRAS, 476, 4592
de Jaeger, T., Zheng, W., Stahl, B. E., et al. 2019, MNRAS, 490, 2799
de Vaucouleurs, G., de Vaucouleurs, A., Corwin, H. G., Jr., et al. 1991, Third Reference Catalogue of Bright Galaxies. Volume I: Explanations and references. Volume II: Data for galaxies between 0h and 12h. Volume III: Data for galaxies between 12h and 24h (Berlin: Springer)
Dessart, L., Audit, E., & Hillier, D. J. 2015, MNRAS, 449, 4304
Dessart, L., & Hillier, D. J. 2005, A&A, 439, 671
Dessart, L., Hillier, D. J., Audit, E., et al. 2016, MNRAS, 458, 2094
Dessart, L., Hillier, D. J., Waldman, R., & Livne, E. 2013, MNRAS, 433, 1745
Dessart, L., John Hillier, D., & Audit, E. 2017, A&A, 605, A83
Eikenberry, S., Elston, R., Raines, S. N., et al. 2006, Proc. SPIE, 6269, 626917
Elias-Rosa, N., Van Dyk, S. D., Li, W., et al. 2010, ApJL, 714, L254
Faran, T., Poznanski, D., Filippenko, A. V., et al. 2014, MNRAS, 445, 554
Farrell, E. J., Groh, J. H., Meynet, G., et al. 2020a, MNRAS, 495, 4659
Farrell, E. J., Groh, J. H., Meynet, G., & Eldridge, J. J. 2020b, MNRAS, 494, L53
Fassia, A., Meikle, W. P. S., Vacca, W. D., et al. 2000, MNRAS, 318, 1093
Filippenko, A. V. 1997, ARA&A, 35, 309
Förster, F., Moriya, T. J., Maureira, J. C., et al. 2018, NatAs, 2, 808
Fox, O. D., Chevalier, R. A., Skrutskie, M. F., et al. 2011, ApJ, 741, 7
Fransson, C., Ergon, M., Challis, P. J., et al. 2014, ApJ, 797, 118
Fransson, C., Lundqvist, P., & Chevalier, R. A. 1996, ApJ, 461, 993
Fraser, M., Takáts, K., Pastorello, A., et al. 2010, ApJL, 714, L280
Freudling, W., Romaniello, M., Bramich, D. M., et al. 2013, A&A, 559, A96
Galbany, L., Hamuy, M., Phillips, M. M., et al. 2016, AJ, 151, 33
Gall, E. E. E., Polshaw, J., Kotak, R., et al. 2015, A&A, 582, A3
Gal-Yam, A. 2017, Handbook of Supernovae (Cham: Springer), 195
Gal-Yam, A., Arcavi, I., Ofek, E. O., et al. 2014, Natur, 509, 471
Garnavich, P. M., & Ann, H. B. 1994, AJ, 108, 1002
Gehrels, N., Chincarini, G., Giommi, P., et al. 2004, ApJ, 611, 1005
Gerardy, C. L., Fesen, R. A., Nomoto, K., et al. 2002, ApJ, 575, 1007
González, M., Audit, E., & Huynh, P. 2007, A&A, 464, 429
González-Gaitán, S., Tominaga, N., Molina, J., et al. 2015, MNRAS, 451, 2212
Graham, M. J., Kulkarni, S. R., Bellm, E. C., et al. 2019, PASP, 131, 078001
Graur, O., Bianco, F. B., Modjaz, M., et al. 2017, ApJ, 837, 121
Graziani, R., Courtois, H. M., Lavaux, G., et al. 2019, MNRAS, 488, 5438
Greiner, J., Bornemann, W., Clemens, C., et al. 2008, PASP, 120, 405
Groh, J. H. 2014, A&A, 572, L11
Groh, J. H., Meynet, G., Georgy, C., & Ekström, S. 2013, A&A, 558, A131
Gutiérrez, C. P., Anderson, J. P., Hamuy, M., et al. 2017, ApJ, 850, 90
Gutiérrez, C. P., Pastorello, A., Jerkstrand, A., et al. 2020, MNRAS, 499, 974
Heger, A., Fryer, C. L., Woosley, S. E., Langer, N., & Hartmann, D. H. 2003, ApJ, 591, 288
Hillier, D. J., & Miller, D. L. 1998, ApJ, 496, 407
Hosseinzadeh, G. 2020, griffin-h/lightcurve_fitting v0.1.0, Zenodo, doi:10.5281/zenodo.3908580
Hosseinzadeh, G., Valenti, S., McCully, C., et al. 2018, ApJ, 861, 63
Hsiao, E. Y., Phillips, M. M., Marion, G. H., et al. 2019, PASP, 131, 014002
Huang, C., & Chevalier, R. A. 2018, MNRAS, 475, 1261
Inserra, C., Turatto, M., Pastorello, A., et al. 2011, MNRAS, 417, 261
Jerkstrand, A. 2017, Spectra of Supernovae in the Nebular Phase (Berlin: Springer), 795
Jerkstrand, A., Fransson, C., Maguire, K., et al. 2012, A&A, 546, A28
Kalberla, P. M. W., Burton, W. B., Hartmann, D., et al. 2005, A&A, 440, 775
Khazov, D., Yaron, O., Gal-Yam, A., et al. 2016, ApJ, 818, 3
Kourkchi, E., Courtois, H. M., Graziani, R., et al. 2020, AJ, 159, 67
Krühler, T., Küpcü Yoldaş, A., Greiner, J., et al. 2008, ApJ, 685, 376
Kulkarni, S. R. 2013, ATel, 4807, 1
Kuncarayakti, H., Anderson, J. P., Galbany, L., et al. 2018, A&A, 613, A35
Law, N. M., Kulkarni, S., Ofek, E., et al. 2009, BAAS, 41, 418
Leonard, D. C., Filippenko, A. V., Barth, A. J., & Matheson, T. 2000, ApJ, 536, 239
Levesque, E. M., Massey, P., Olsen, K. A. G., et al. 2005, ApJ, 628, 973
Li, W., Leaman, J., Chornock, R., et al. 2011, MNRAS, 412, 1441
Liu, Q. Z., Hu, J. Y., Hang, H. R., et al. 2000, A&AS, 144, 219
Matheson, T., Filippenko, A. V., Ho, L. C., Barth, A. J., & Leonard, D. C. 2000, AJ, 120, 1499
Meynet, G., Chomienne, V., Ekström, S., et al. 2015, A&A, 575, A60
Meynet, G., Ekstrom, S., Maeder, A., et al. 2013, in Lecture Notes in Physics, Vol. 865, ed. M. Goupil et al. (Berlin: Springer), 3
Moriya, T., Tominaga, N., Blinnikov, S. I., et al. 2011, MNRAS, 415, 199
Moriya, T. J., Maeda, K., Taddia, F., et al. 2013, MNRAS, 435, 1520
Morozova, V., Piro, A. L., & Valenti, S. 2017, ApJ, 838, 28
Morozova, V., Piro, A. L., & Valenti, S. 2018, ApJ, 858, 15
Mukai, K. 1993, Legacy, 3, 21
Nicholl, M., Guillochon, J., & Berger, E. 2017, ApJ, 850, 55
Niemela, V. S., Ruiz, M. T., & Phillips, M. M. 1985, ApJ, 289, 52
Ofek, E. O., Zoglauer, A., Boggs, S. E., et al. 2014, ApJ, 781, 42
Oke, J. B., Cohen, J. G., Carr, M., et al. 1995, PASP, 107, 375
Osterbrock, D. E., & Ferland, G. J. 2006, Astrophysics of Gaseous Nebulae and Active Galactic Nuclei (Sausalito, CA: Univ. Science Books)
Pastorello, A., Crockett, R. M., Martin, R., et al. 2009, A&A, 500, 1013
Pastorello, A., Smartt, S. J., Botticella, M. T., et al. 2010, ApJL, 724, L16
Pastorello, A., Wang, X. F., Ciabattari, F., et al. 2016, MNRAS, 456, 853
Patat, F., Barbon, R., Cappellaro, E., et al. 1994, A&A, 282, 731
Perley, D. A. 2019, PASP, 131, 084503
Phillips, M. M., Simon, J. D., Morrell, N., et al. 2013, ApJ, 779, 38
Poznanski, D., Prochaska, J. X., & Bloom, J. S. 2012, MNRAS, 426, 1465
Pozzo, M., Meikle, W. P. S., Fassia, A., et al. 2004, MNRAS, 352, 457
Quimby, R. M., Wheeler, J. C., Höflich, P., et al. 2007, ApJ, 666, 1093
Rabinak, I., & Waxman, E. 2011, ApJ, 728, 63
Rayner, J. T., Toomey, D. W., Onaka, P. M., et al. 2003, PASP, 115, 362
Reichart, D., Nysewander, M., Moran, J., et al. 2005, NCimC, 28, 767
Rockosi, C., Stover, R., Kibrick, R., et al. 2010, Proc. SPIE, 7735, 77350R
Rubin, A., & Gal-Yam, A. 2016, ApJ, 828, 111
Ryder, S. D., Kool, E. C., Stockdale, C. J., et al. 2017, ATel, 10147, 1
Sana, H., de Mink, S. E., de Koter, A., et al. 2012, Sci, 337, 444
Sanders, N. E., Soderberg, A. M., Gezari, S., et al. 2015, ApJ, 799, 208
Sapir, N., & Waxman, E. 2017, ApJ, 838, 130
Schlafly, E. F., & Finkbeiner, D. P. 2011, ApJ, 737, 103
Schlegel, E. M. 1990, MNRAS, 244, 269
Shappee, B. J., Prieto, J. L., Grupe, D., et al. 2014, ApJ, 788, 48
Shivvers, I., Groh, J. H., Mauerhan, J. C., et al. 2015, ApJ, 806, 213
Silverman, J. M., Nugent, P. E., Gal-Yam, A., et al. 2013, ApJS, 207, 3
Simcoe, R. A., Burgasser, A. J., Schechter, P. L., et al. 2013, PASP, 125, 270
Smartt, S. J. 2009, ARA&A, 47, 63
Smith, K. W., Smartt, S. J., Young, D. R., et al. 2020, PASP, 132, 085002
Smith, N., Kilpatrick, C. D., Mauerhan, J. C., et al. 2017, MNRAS, 466, 3021
Smith, N., Li, W., Filippenko, A. V., & Chornock, R. 2011, MNRAS, 412, 1522
Smith, N., Silverman, J. M., Filippenko, A. V., et al. 2012, AJ, 143, 17
Sorce, J. G., Tully, R. B., Courtois, H. M., et al. 2014, MNRAS, 444, 527
Spiro, S., Pastorello, A., Pumo, M. L., et al. 2014, MNRAS, 439, 2873
Stritzinger, M., Taddia, F., Fransson, C., et al. 2012, ApJ, 756, 173
Svirski, G., Nakar, E., & Sari, R. 2012, ApJ, 759, 108
Taddia, F., Stritzinger, M. D., Fransson, C., et al. 2020, A&A, 638, A92
Takáts, K., & Vinkó, J. 2012, MNRAS, 419, 2783
Tartaglia, L., Pastorello, A., Sollerman, J., et al. 2020, A&A, 635, A39
Tartaglia, L., Sand, D., Valenti, S., et al. 2017, ATel, 10058, 1
Tartaglia, L., Sand, D. J., Valenti, S., et al. 2018, ApJ, 853, 62
Terreran, G., Jerkstrand, A., Benetti, S., et al. 2016, MNRAS, 462, 137
The Astropy Collaboration, Price-Whelan, A. M., Sipőcz, B. M., et al. 2018, AJ, 156, 123
Tonry, J. L. 2011, PASP, 123, 58
Tully, R. B., & Courtois, H. M. 2012, ApJ, 749, 78
Tully, R. B., Courtois, H. M., Dolphin, A. E., et al. 2013, AJ, 146, 86
Turatto, M., Benetti, S., & Cappellaro, E. 2003, in From Twilight to Highlight: The Physics of Supernovae, ed. W. Hillebrandt & B. Leibundgut (Berlin: Springer), 200
Valenti, S., Howell, D. A., Stritzinger, M. D., et al. 2016, MNRAS, 459, 3939
Valenti, S., Sand, D., Pastorello, A., et al. 2014, MNRAS, 438, L101
Waxman, E., & Katz, B. 2017, Handbook of Supernovae (Berlin: Springer), 967
Yang, S., Sand, D. J., Valenti, S., et al. 2019, ApJ, 875, 59
Yang, S., Valenti, S., Cappellaro, E., et al. 2017, ApJL, 851, L48
Yaron, O., Perley, D. A., Gal-Yam, A., et al. 2017, NatPh, 13, 510